
Imperial College

London

Platform for Microrobot Navigation

Nafiseh Vahabi

A thesis submitted in partial fulfilment of the requirements for the degree of
MRes in Medical Robotics and Image Guided Intervention and for the Diploma of

Imperial College

Imperial College London

Department of Surgery and Cancer

September, 2014

Dr. Henry Ip

Dr. Vincenzo Curto

Prof. Guang-Zhong Yang

Acknowledgements

First and foremost, I wish to express my sincere thanks to my supervisor Prof. Yang for his valuable guidance and high level supervision during my MRes course.

I am especially grateful to my supervisors Dr. Henry Ip and Dr.Vincenzo Curto for their assistance and suggestions throughout this project. My thanks to both of you for helping me to improve my final presentation, reading the draft of my thesis and providing me with your valuable feedback.

I would like to thank Dr. Ebubekir Avci for helping me to take images of my fabricated structures with Scanning Electron Microscope.

I would like to thank the course leader Dr. Daniel Elson for all his organisation and arrangements for the MRes students to make this course an enjoyable one.

I am most grateful to my husband Ali for all his love, support and help during my study. Thanks for me advising me with my , for your patience and most importantly caring for our children during this pressured time. This thesis would not have been possible without you.

I would like to thank my daughter Parmin and my son Ario who always give me their love and joy.

Finally, my special thanks to my parents and my brother for all their encouragement and support during the project.

Contents

List of Figures	iii
List of Tables	iv
List of Acronyms	v
1 Introduction	1
1.1 Literature review	4
1.1.1 Bioinspired microrobots	4
1.1.1.1 Flagella style microrobots	4
1.1.1.2 Plant-based microrobots	10
1.1.2 Actuation methods	12
1.1.3 Fabrication methods	13
2 Methods	17
2.1 Microrobot design	17
2.2 Microrobot fabrication	19
2.2.1 Nanoscribe	20
2.2.2 Scanning Electron Microscope (Scanning Electron Microscope (SEM)) . . .	22
2.3 Simulation	24
2.3.1 Modelling helical propulsion	25
2.3.1.1 Resistive force theory for microrobot with two degrees of freedom	27

2.3.1.2	Resistive force theory for six degrees of freedom	30
2.3.1.3	Regularized Stokeslet method	37
2.3.1.4	Slender body theory	39
2.3.2	Microrobot actuation	43
3	Results	50
3.1	Simulation	50
3.2	Fabrication	55
4	Discussion	62
5	Conclusion and future work	64
	Bibliography	66

List of Figures

1.1	Project workflow	3
1.2	Propulsion mechanism of mastigonemes flagellum	4
1.3	Micro-structures and microdevices	5
1.4	Helical microswimmers design	5
1.5	Effect of gravity on swimming microrobot	7
1.6	Effect of frequency on microswimmer's behaviour	8
1.7	Drilling motion of a nanotube	9
1.8	The prototype of microhelical device	10
1.9	Xylem's shape in different plants	11
1.10	plant-based microrobot	12
1.11	Direct lasor writing	14
2.1	Different helical designs	18
2.3	Fabrication process overview	19
2.2	Variable pitch helix design	20
2.4	Nanoscribe workflow	21
2.5	Scanning Electron Microscope	21
2.6	Fabrication process overview	24
2.7	Helix parameters	26
2.8	Microrobot filament motion	27
2.9	A motion of helical segment	27

2.10	Helical microrobot configuration with a magnetic spherical head	30
2.11	RSM and SBT	40
2.12	Construction details of direction of the microswimmer	46
3.1	Simulation framework	52
3.2	Simulation domain	52
3.3	Rotational velocity vs. helix angle	53
3.4	Rotational velocity vs. helix pitch	54
3.5	Rotational velocity vs. helix rediu	54
3.6	Rotational velocity vs. helix filament radius	55
3.7	Rotational velocity vs. translational velocity	56
3.8	Microhelix first position	57
3.9	Variable pitch helix	58
3.10	Circle base helix	58
3.11	Fabricated structures	59
3.12	Rectangle based structures	60

List of Tables

1.1	Summery of microrobots's design, locomotion and fabrication	16
3.1	Simulation model configuration	51
3.2	Modelling Simulation Componets	51

List of Acronyms

SBT Slender Body Theory

FBMS Fixed-beam Moving-sample

gw1 General Writing Language

MPC Magnetic Polymer Composite

MBFS Moving-beam Fixed-sample

RFT Resistive Force Theory

RSM Regularized Stokeslet Method

SEM Scanning Electron Microscope

stl STereoLithography

Abstract

Microrobots provide the opportunity to develop a system, the size of a bacteria, capable of swimming in a controllable manner in a high viscous fluid and which could perform delicate tasks such as targeted drug delivery in a medical application. Furthermore, microrobots have benefited from fabrications technology, which makes them biocompatible. The structures and functions of microorganisms make them a suitable reference point for the design of microrobots. This is because the flagella propulsion of microorganisms such as E.coli can be used to provide an efficient approach for modelling micro swimmers locomotion method in low Reynolds number regime. Microrobots demonstrated precise and controllable movements under low strength magnetic field. In this study we reviewed a range of bio mimetic microrobots in terms of their design, fabrication, propulsion method in the fluid environment. The key characteristics of the helical shape microswimmers were optimised and the new design of helical microrobot is presented. The new design is demonstrated the microrobot with the variable pitch that is satisfied the fabrication requirement.

The three propulsion methods studied were; Resistive Force Theory, Regularised Stokeslet Method and Slender Body Theory. The last two methods have not previously been used for remotely controlled microrobots. We provide the simulation platform for the swimming microrobot in a high viscose fluid. The simulation algorithm takes a desired translational velocity of a microrobot and calculates the electric current required to generate a dynamic magnetic field.

Chapter 1: Introduction

Robotic surgery has demonstrable advantages such as reducing pain and discomfort and minimising scarring after invasive surgery. As robotic technology continues to move towards miniaturisation, the idea of using a microrobot for medical applications such as cardiovascular surgery, also becomes more attractive [1] The potential applications of a microrobot can be classified into two main categories; in vivo and in vitro applications. Some in vivo examples are drug delivery, delivery of hyperthermia for cancer treatment and ablation of material. In vitro applications can involve microfluid control, cell characterisation and manipulation [2].

Magnetically actuated helical microswimmers have been reported as a safe microdevice for biomedical applications [3]. However, there are number of challenges such as the issue of biocompatibility and the material used to make a microrobot, which needs to be considered carefully for in vivo application[4]. Research into swimming microrobots has identified two primary difficulties, namely the power source and a suitable locomotion method. This is because there are many cells, proteins and fibres in biofluid that prevent the motion of the microrobots [5]. The extremely small size of the microrobot and the complex biofluid environment makes the design aspect a very challenging one. Furthermore, the design of a microrobot will depend on its application and the desired task to be performed. Artificial bacteria flagella is a popular microrobot inspired by nature [4]. They have helical shape, are composed of magnetic material and are capable of mimicking the three-dimensional motion of the bacteria in a high viscous fluid.

The reason for developing a simulation platform for microroswimmers navigation is to analyse their characteristic and behaviour under low magnetic field. A few numbers of parameters has a key role on designing the helical shape microswimmer. The simulation challenge can be divided into two main parts; propulsion mechanism of the microrobot and actuation method. The popular method, Resistive Force Theory (RFT), describes the motion of the helix object in a low number regime and is applied by most helical microswimmers's algorithms[4]. In this project, we studied two more propulsion methods for the remotely controlled helical microswimmers in a dynamic magnetic field, Regularized Stokeslet Method (RSM) and Slender Body Theory (SBT). An actuation method of a magnetic microrobot can be either force driven or torque driven [6]. Fabrication of a microdevice has been a considerable challenge for some time [6], which has now been overcome by fabrication methods such as 3D laser lithograph.

In summary, part of the algorithms developed for the propulsion mechanism of the microswimmers and their actuation technique, were based on Mahoney et al.'s research. Two new propulsion methods for the helical microswimmers were used in the Rodenborn et al.'s work. This involved a reversible speed-variable motor such as a micro metal gear motor being used to rotate the microswimmer. In this study, these two propulsion mechanisms were applied to the microswimmers that are then controlled remotely by a magnetic field. Therefore, the algorithm has taken the desired translational velocity as an input and produced the rotational velocity as an output. By knowing the rotational velocity, we will be able to compute the electric current required to produce the desired translational velocity. In addition, the new design is developed and printed for the helix using a variable pitch in the helix design rather than a constant pitch to satisfy the fabrication process.

A literature review on the different aspects of microrobots is presented in chapter 1. An overview of the main microrobot designs are summarised in the table 1.1. Section 2.1 demonstrates the

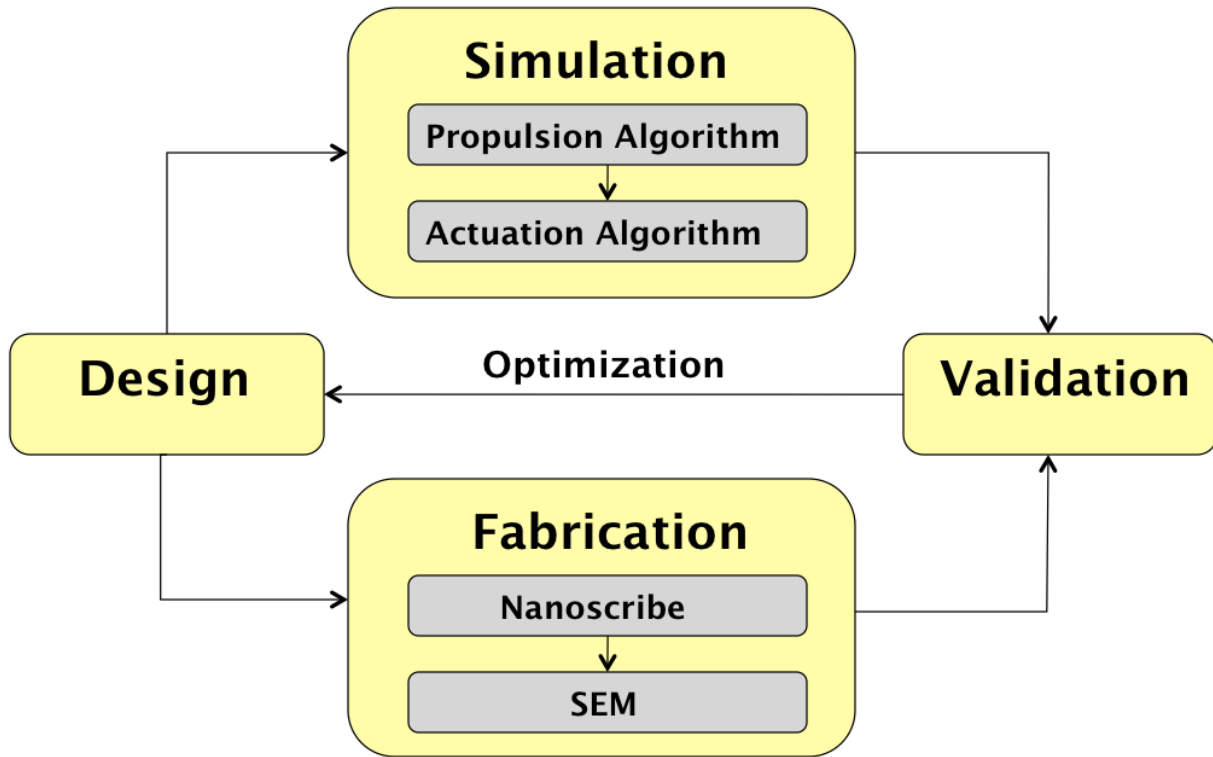


Figure 1.1: Project workflow. The project started by designing microhelix and followed by parallel work on the fabrication and simulation. The final structures were analysed and optimised in terms of their design.

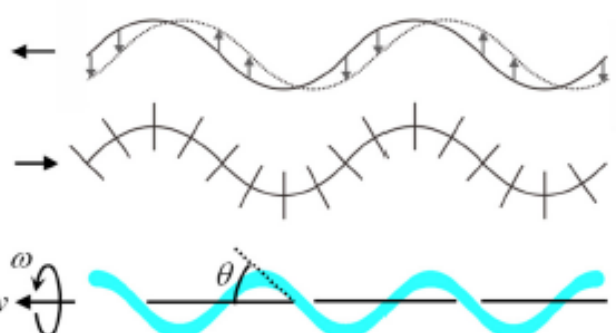
details of the effective parameters on microrobot's design and optimises them to characterise the new design for a helix shaped microrobot. The major part of this project involves studying, solving and implementing the simulation methods described in section 3.2a. Whilst the mechanism of both methods are explained in the section 2.3.2, we only implemented the torque driven actuation method in this study. Section 1.1.3 presents a brief history of the fabrication techniques and section 2.2 describes the fabrication method applied in this study. Chapter 3 provided the results of this work in terms of both simulation and fabrication. The key issues are discussed in chapter 4 and conclusion and potential future work is described in chapter 5. An overview of the entire system is shown in diagram 1.1.

1.1 Literature review

1.1.1 Bioinspired microrobots

One of the most challenging aspects of designing a robot on a very small scale such as a nanorobot is simplicity. The reason is, integration between various components will become unfeasible on such a small scale if the design is complex. Hence the development of the nanorobot or even micro-robot should be based on the essential functionality, avoiding any unnecessary components [9]. By learning from nature and mimicking the structure of live organisms, the successful scientific applications were created [6]. The following section describes a few examples of swimming microrobots that were imitated from nature.

Reynolds number To understand how micro-organisms swim in a fluidic environment, it is essential to study their propulsion mechanism. In the fluidic regime the Reynold number



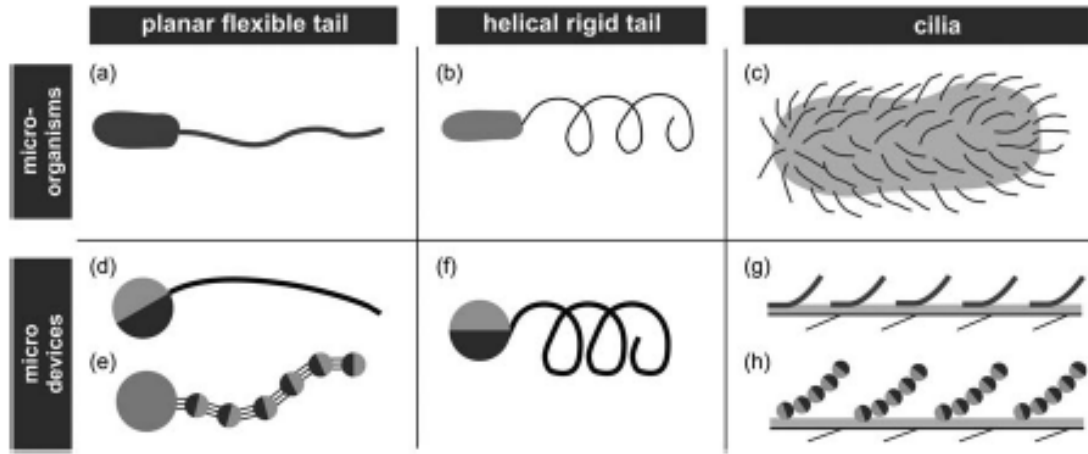


Figure 1.3: Micro-structures and microdevices. The illustration of both flagellum and cilia shapes and microdevices mimicked the flagellum and cilia structures [5].

(Re) has a substantial effect on a microdevice locomotion [3]. The Reynolds number describes the ratio of the inertial forces versus viscous forces according the following formula;

$$Re = \frac{UL\rho}{\mu} \quad (1.1)$$

Where U is velocity, L is characteristic length, ρ is the density and μ is viscosity of the fluid.

1.1.1.1 Flagella style microrobots

Helical flagella and cilia are two well-known microswimmers in nature that have had their functionality employed for motion generation in artificial microrobots (Figure 1.3) [9].

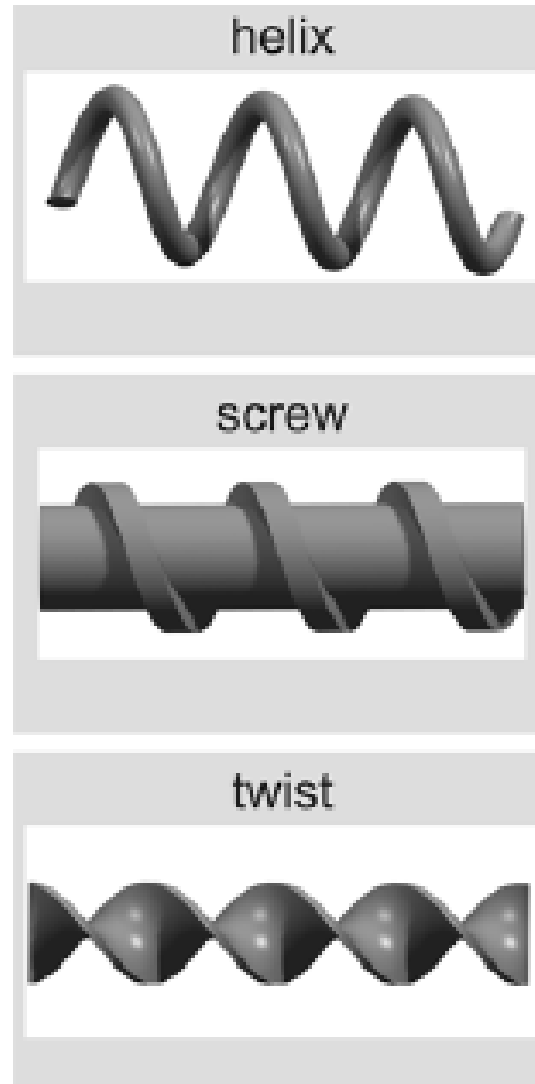
In 2007, Bell [9] presented the first artificial bacteria flagellum microrobots and then Zhang characterised them in 2009 [9]. This microrobot was formed of two components; a rigid helical tail and a soft magnetic metal head.

The head diameter was $2.8\mu m$ and its length was $30 - 100\mu m$. Since then, other scientists proposed a slightly different design , that mostly have the rigid helical tail shape. However, in some cases the magnetic materials is used in the tail of the device rather than the head [9].

The helical rotation of flagella and the travelling wave beat of cilia are two non-reciprocal propulsion mechanisms in microorganisms. Mimicking a rotating flagellum at low Reynolds number to generate an adequate torque to overpower the high viscous drag requires two main elements; a rotary motor and a power source [6].

An electromagnetic rotary motor can be used in designing a helical flagella style microrobot that requires a considerable current. However piezoelectric rotary motors are an alternative option that are appropriate for miniaturisation but necessitate high input voltage. Hence, designing a microrobot with a combination of an onboard power source and a motor is a challenging task [6].

Another design of microswimmers was inspired by the function of magtigonemes in nature [10]. A smooth flagellum propels against the direction of the flagella's propagation wave. However, the flagellum covered by magtigoneme



propels in the same direction as the flagellum wave (Figure 1.2). Mimicking the structure of flagellum and using 3D lithography and electron beam evaporation formed the fabrication method in these microswimmers. The anisotropic viscous drag on the flagella is an important fact for locomotion in low Reynolds number fluid. Flagella movement in the opposite direction of the flagella wave is because the viscous drag coefficient perpendicular to the flagella is greater than the viscous drag coefficient parallel to the flagella [10].

The artificial smooth flagellum is powered by an external magnetic field. The rotating field, i.e. rotational frequency, field strength and angles that defined the rotational axis is controlled by the current in the external coil. The helical microrobots rotate synchronously with the rotation of the magnetic field and move forward and backward accordingly [10]. The displacement of the microswimmer along the rotational axis can be measured and the result used to calculate the average velocity of the swimmers. There is a linear relationship between an input field frequency and swimming speed. According to their result [10], a propulsive force generated by the mastigoneme is in opposite direction of the force generated by the main helical filament. However, this velocity is only valid if the external force is zero. The proposed design [10] is rigid and an external stimulus may be used to regulate the swimming speed and direction if the swimmer can fold and unfold their structure.

There are three common shapes of microrobots based on the rotary action; a helix, a screw and a twisted ribbon shape around its axis (Figure 1.4). For the purpose of drilling into solid matter such as biological tissue the screw and helix design would be more appropriate. The rotational motion of helical micro swimmers is one of the most effective propulsion methods in the low Reynolds number scenarios because it leads to translational motion. Microrobots with the microspheres structure perform similarly to the helical swimmers and are capable of swimming in the flowing

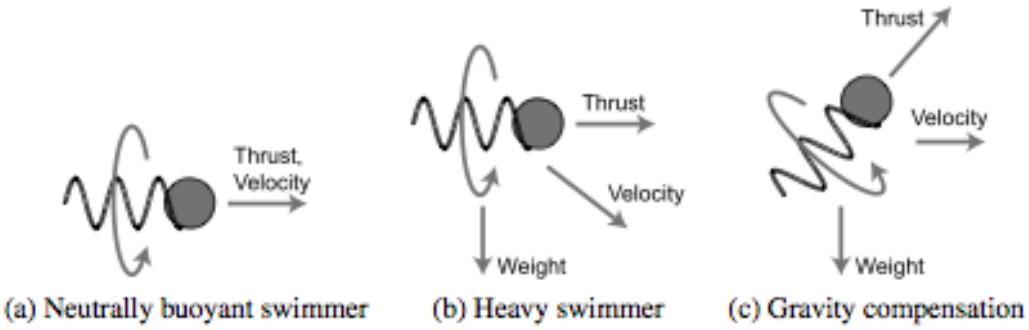


Figure 1.5: The effect of the gravity on the microrobot motion direction and gravity compensation [7].

liquid within the micro-fluidic channel [11].

There are two main factors that affect the movements of the microrobot in the external magnetic field; low coercivity and high saturation magnetization. Also, the motion of the microrobot is related to its size given the same magnetic field strength and as such, by increasing the size of the microrobot with the inflexible magnetic material volume, the velocity will decrease [11]. The surface friction and the drag forces are two resistive forces that impede the microrobot's motion. Hence, the input magnetic force must be sufficient to overcome these forces for microrobot manipulation. Furthermore, the weight of the microrobot requires gravity compensation in the z-direction by the magnetic field. The navigation methodology should compensate for gravity to avoid sinking and enable velocity to be controlled wirelessly. Mahoney et al. described an algorithm for helical microswimmers velocity control plus gravity compensation. In the proposed model the correct pitch angel and rotation speed is calculated to achieve the commanded velocity (Figure 1.5).

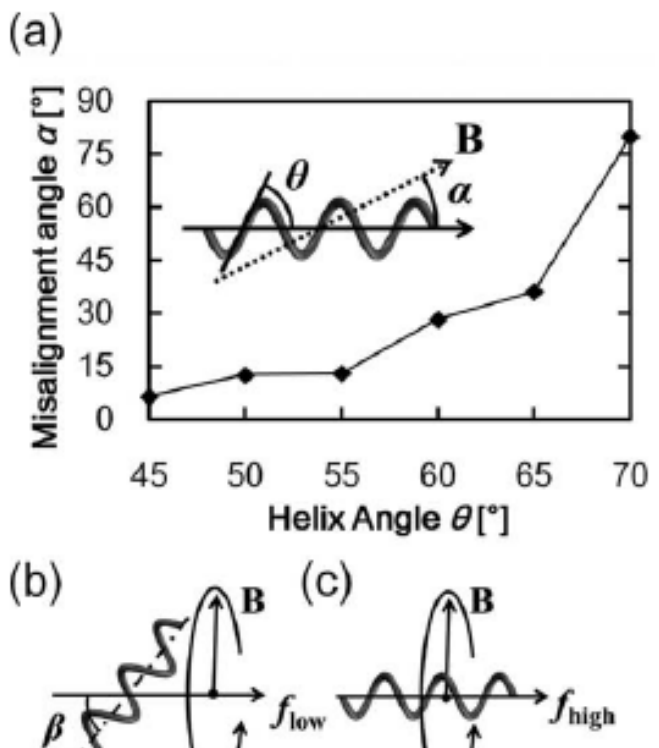
A magnetic field can be used for controlling teams of microrobots as well as a single one. Kim et al. proposed a method that used a combination of two magnetic materials to attain on/off magnetization of each microrobot. The overall control of the group of microrobots was achieved by managing the magnetization state of each microrobot. In addition, a second technique has been

developed for three-dimensional motion of the team of microrobots in a fluidic environment. In the latter method, each microrobot is designed in such a way that it uniquely responds to the input magnetic field. Therefore, several microrobots can provide feedback position control in 3D system [11]. An untethered spherical magnetic micromanipulator creates a locally induced rotational fluid flow gradient. The created rotational flow propels micro-objects in the flow area. A team of microrobots could perform a complex task in micro-transport and micro-assembly [11].

In another study [12], a helical microrobot was designed to swim in a low Reynolds number. Two designs are selected to run the experiment; the first one is a bare helical structure and the second one is the helical shape with the microholder attached at the end. Both designs will generate the corkscrew motion in a fluid environment when the magnetic field is about few mili Tesla. The second design (device with the microholder) is capable of transporting a microobject accurately to the target [12].

In Tottori et al.'s study eight designs of microrobots were proposed and tested. The uniform static magnetic field was used to explore the magnetic shape anisotropy and the magnetic actuation was monitored in the rotating magnetic field. In the static magnetic field the set of microrobots had helical angles θ ranging from 45° to 70° when suspended in the deionised water.

This showed (Figure 1.6) that a smaller helix angle θ results in a reduced misalignment angle α because microrobots longest axes will be aligned to the direction of the external magnetic field. However in a helical microrobot with larger helix angles (θ), the magnetization direction would change to the radial axes of the helix [12]. In the rotating magnetic field, the micro helical swimmer exhibits dif-



ferent behaviours depending on the strength of the applied frequency in the fixed magnetic field. At low frequencies the micro helix oscillated around the helical axes, however the oscillating behaviour changed to the corkscrew motion after increasing the applied frequency in the magnetic field. This is similar to characteristics of microrobots with an incorporated microholder [12].

The velocity of helical micro swimmers depends on their size and shape. A linear relationship was observed between the input frequencies and swimming velocity of the micro swimmers. The outcome of the comparison between three microhelixs with the same helix angles showed that the microhelix with the greatest diameter has the highest speed, in accordance with the following formula;

$$U = \frac{(C_n - C_1) \sin \theta \cos \theta}{2(C_n \sin^2 \theta + C_1 \cos^2 \theta)} (d\varpi) \quad (1.2)$$

Where C_n is a drag coefficient perpendicular to the filament and C_1 is a drag coefficient parallel to the filament. ϖ is the rotational frequency and d is the rotational diameter of the helix [12].

The important role of helix angle in the magnetization structure of helical micro swimmers was confirmed by Peyer et al. [13], who used direct laser writing (DLW) as a fabrication method on a Magnetic Polymer Composite (MPC). The MPC are non-cytotoxic and showed super paramagnetic characteristic because magnetic material was already included in the polymer.

The relationship between the torque T , the drag force F , the object's velocity v and rotational

speed ω is linear and modelled by 6×6 resistant matrix as below;

$$\begin{bmatrix} F \\ T \end{bmatrix} = \begin{bmatrix} A & B \\ C & D \end{bmatrix} \begin{bmatrix} \nu \\ \omega \end{bmatrix}$$

Where A , B and D are matrices 3×3 and only depend on the object's geometry and fluid velocity.

In the study performed by Purcell [14] it has been proved matrices B and C are equal ($B = C$) for a typical flagellum.

There are few methods in use to model the resistance matrices and low Reynolds flow such as the method of regularized stokeslets, the boundary element method and the method of fundamental solution . In designing a micro-robot the main parameters required to concentrate on are the helicity angle ψ , the helix radius R , the pitch p and the filament radius r as illustrated in Figure 1.8 part (c).

Magnetic actuated microrobot is divided into two categories; torque driven microrobot and force driven microrobots. The micro robot using the torque-driven method is more favourable than the force-driven method because their rotation is based on applying torque rather than a force to pull the device [13].

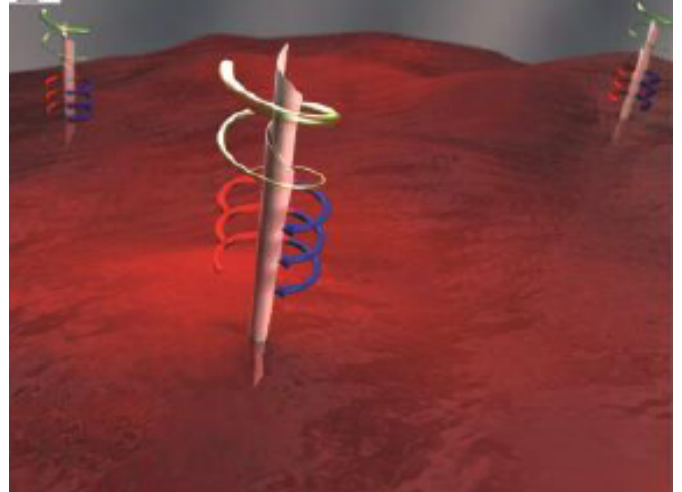


Figure 1.7: Demonstrating the drilling motion of the nanotubes under rotating magnetic field [15].

Another approach for powering a micro robot is using the catalytic conversion of chemical energy into mechanical energy (Figure 1.7). In this method, the catalyst accelerates the consumption of hydrogen peroxide and helps the self-propulsion of micro robot to pump the fluid to transport cells and colloidal particles [15]. The catalytic tube is fabricated with a sub micrometer diameter.

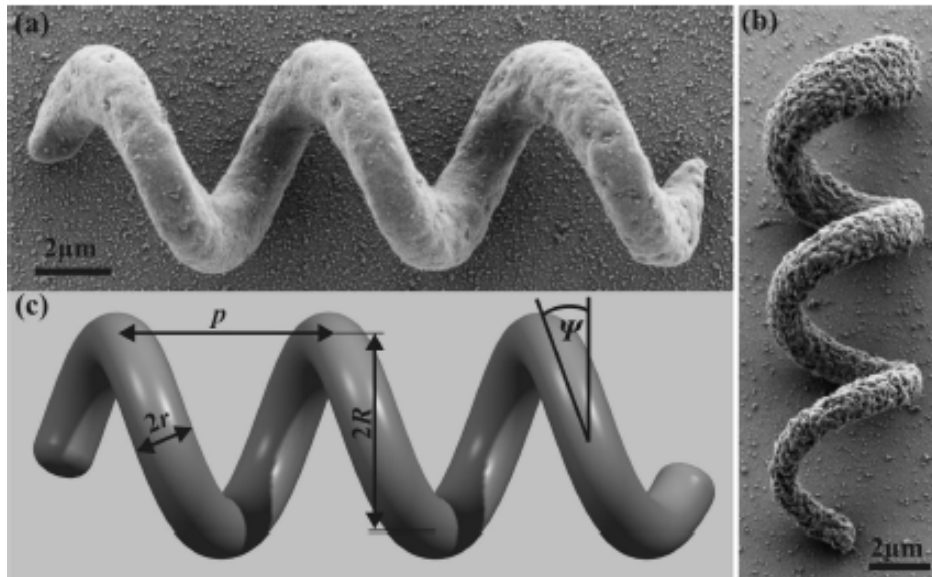


Figure 1.8: The prototype of microhelical device. (a) Scanning electron microscopic image of the micro polymer composite with the 2 vol.% nanoparticle fill factor and (b) 4 vol.% of nanoparticle fill factor. (c) The CAD model shows all the parameters required for the microhelical design [13].

This technique is not applicable for the minimally invasive surgery (MIS) yet because the catalytic material used in the fabrication process of nanotubes is toxic. Hence, biocompatible fuel is required to be developed in order to apply this technique in a live cell environment [15].

Alternatively, the micro driller can be powered and controlled by using an external magnetic field such that changes in the frequency of the rotating magnetic field switch the rotational orientation of the micro tool from the horizontal position to the vertical one. The vertical orientation of the rolled up microtube and its sharp helical design makes the device suitable for drilling into biological tissue. In addition, the micro driller can be used for targeted drug delivery in MIS [15].

1.1.1.2 Plant-based microrobots

The helical microstructures are not limited to having flagellum-like structures and microbots with general cilia-like feature have been designed. Gao et al. observed the helical microstructures that imitates spiral water-conducting vessels of different plants.

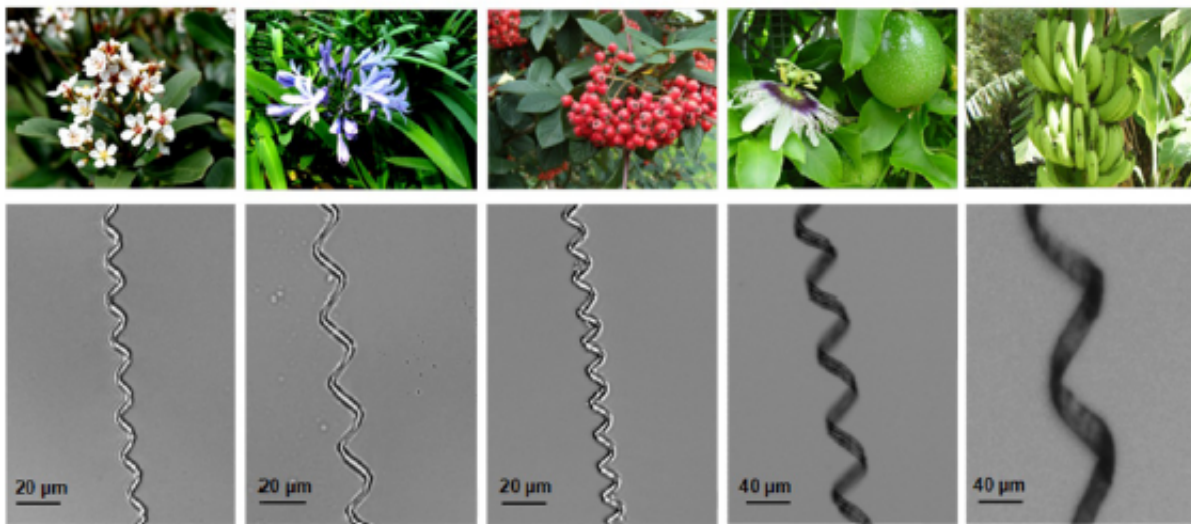


Figure 1.9: The shape of the Xylem in different plants [7].

In order to obtain unstretched spiral vessel several plants were collected and their leaves were macerated and washed with pure water. Tweezers were used to uncover compressed spiral vessels in the planar networks. Leaves were gently scored and two segments were pulled apart to a permanent length to stretch the spiral vessels. These spiral vessel were kept in a glass slides and covered with a thin layer (20nm) of titanium and nickel (80nm) using an E-beam evaporator [7]. The helical vessels were coated in nail polish and baked for 2 minutes to impound the helix and protect the structure. The final product is a photoresist film on glass that was cut into required lengths.

The fabrication process involves coating isolated spiral xylem vessel plant fibres within a (Figure 1.8) thin magnetic layer. Xylem tissue transports the plant's required food such as water and other nutrition from the root to the leaves using capillary action [7]. Use of plant material in this method enables simple three-dimensional microswimmers fabrication and biocompatibility. In addition, the magnetic cover helps to ensure accurate directional control and high-speed propulsion. Therefore, the fabrication processes were extremely simplified as the main component of the helical microswimmers is from nature and more than a million individual micro helicals can be made from a very small section of the plant stalk [7]. Using mechanical stretching can control

geometric variables of the helical vessels such as the pitch and helix angle and hence plenty of helical microswimmers can be reproduced. The final shape of the helical microswimmer is determined mainly by the initial diameter of the unstretched spiral vessel.

The process of stretching helical plant structure was performed via plastic deformation so that the number of helical turns are constant and tensile stretching of the plant fibre stretching is negligible [7].

The method used for precise propulsion control and characterising the locomotion behaviour of the plant-based microswimmers is similar to the method applied in Gao et al. study. According to Gao et al. [9] experiment, the plant-based microswimmers exhibited high speed movement ($85 \mu\text{m}$) in raw biological medium such as pure human serum under the rotating magnetic field. However, their swimming speed in pure water ($90 \mu\text{m}$) was slightly higher than human serum.

Hence, an increased velocity of the biological fluid has a minor effect on the plant-driven microswimmers, which is an important advantage of this microdevice over the common micro-robots

1.1.2 Actuation methods

The actuation method for swimming micro-robot should meet two main criteria in order to be applicable. The method needs to be appropriate in the fluid environment and can be applied in the micro scale. One approach was using tethered and onboard motor to an exter-

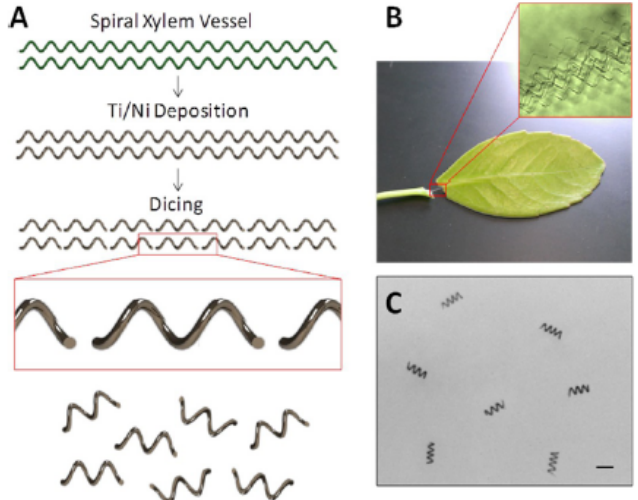


Figure 1.10: (A) The stages were required to make a plant-based microrobot. (B) A microscopic image of the a xylem helical structure [9].

nal power source to actuate the microrswimmers, but this approach will not be realistic in micro scale. Therefore, using the propulsion mechanism of natural swimmers such as flagellum demonstrated a successful result [5].

Another approach is using electrochemical decomposition for microrobot locomotion. The mechanism of these types of artificial microdevice is similar to bacteria as both harvest the required energy from their environment. In that case, the environment contains chemical material such as hydrogen peroxide to make the electrochemical reaction. The successful application of these catalyst microdevice in vitro is reported for cell transportation. However, this approach will not be suitable for in vivo cases where the chemical material may harm the human body [5].

Therefore, the idea of using magnetic field for the microrobot actuation satisfied both requirements. Applying the low strength magnetic field is harmless for the human body and that can be used within fluidic environment. So it is possible to have microswimmers in the fluid environment and to control them remotely. However, there are still challenges with using a magnetic field as an actuation method. The magnetic field will decay fast by increasing the distance from the magnetic source. Thus, that factor needed to be considered when preparing the set up for actuated microrobot [5].

The microrobot actuation by magnetic field can be force driven or torque driven. In the case of the torque driven, the magnetized microrobot experiences a torque that perform to align its magnetization with the external magnetic field. The magnetic torque and force are formulated as follow;

$$\mathbf{T}_m = V \mathbf{M} \times \mathbf{B} \quad (1.3)$$

$$\mathbf{F}_m = V(\mathbf{M} \nabla) \mathbf{B} \quad (1.4)$$

Where $\mathbf{T}_m[N.m]$ is torque, $\mathbf{F}_m[N]$ is force, $\mathbf{M}[A.m^{-1}]$ is magnetization, $V[m^3]$ is volume of a magnetized object and $\mathbf{B}[T]$ is the magnetic field. If we have a hard magnet, \mathbf{M} becomes a constant or it can be a function of the geometry of the object and applied field. In the uniform magnetic field, there is no force and microrobot just experiences the torque until the magnetization \mathbf{M} is collinear with the magnetic field. At this point, there is no torque and the microswimmer remains stationary. Thus, a magnetic field is required to go through spatial or temporal changes to generate a continuous actuation. This can be performed by rotating the helmholtz coils or generating a dynamic magnetic field by using AC current [5].

1.1.3 Fabrication methods

Historically, the fabrication of the microrobot was the main problem to be resolved, but micro-scale fabrication methods offer a feasible solution [9]. In 2007, the first artificial bacteria flagella was fabricated based on thin-film deposition and self-scrolling methods [4]. They used InGaAs/GaAs bilayer for fabricating helical tail and Ni for actuation microrobot's head. The similar fabrication method employed by Zhang in 2009 with the addition of a Cr layer between the microrobots' tail and its head [4]. An improved adhesion of microrobot was the result of adding Cr layer.

3D laser direct writing (DLW) and electron beam decomposition are methods used since then. A typical fabrication process consists of two stages. Initially, the core structure of the artificial helical microswimmer is printed using 3D lithography, following which electron beam evaporation is used for ferromagnetic thin film coating [10]. Performance of each microswimmer (with different design) can be imaged by the scanning electron microscope (SEM). After the fabrication process is completed, the next step is to release the structure into deionised water using the tungsten probe. The tank with deionised water is installed in the middle of the three-axis Helmholtz setup.

To improve biocompatibility for in-vivo applications, the microrobot can be covered with a thin

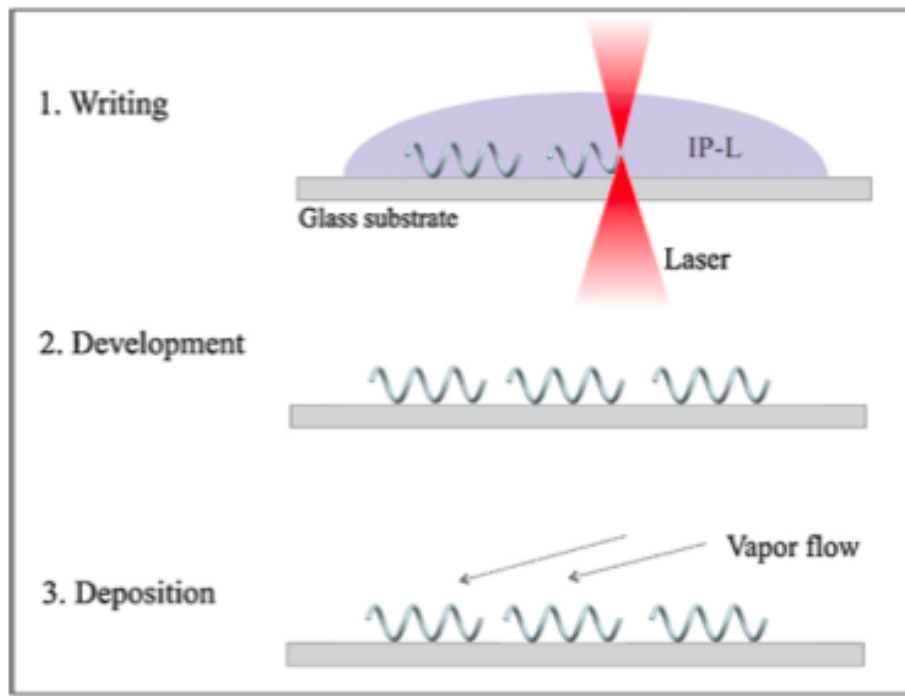


Figure 1.11: DLW steps. step 1 is writing helical microrobots, in step 2 microrobots were developed in isopropyl alcohol and step 3 is coating them by a layer of Ni and Ti. [16].

layer of titanium. In addition, the microrobot's structure was layered with nickel for the purpose of magnetic actuation.

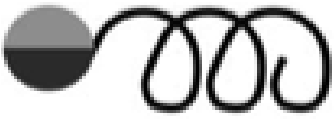
Qiu et al. [16] reported a successful application of helical microrobots for drug delivery were known as “smart” drug carriers. Again, they used DLW for the fabrication method as shown in the Figure 1.11.

The smart drug carriers were coated in a layer of temperature-sensitive liposomes which is composed of a lipid bilayer and was proposed for cancer therapy in local hyperthermia treatments [16].

The main component of temperature-sensitive liposomes is Dipalmi- toylphosphatidylcholine (DPPC) which transforms from solid to liquid gel at the $41^{\circ}C$ and released encapsulated drugs.

Qiu et al. [4] used commercially available material such as ORMOCOMP for fabrication of helical microrobots in their recent experiment. ORMOCOMP is a biocompatible photoresist which can improve the potential use of microrobots for in vivo applications because it supports viability, cell

proliferation and normal morphology of various cell lines. For the purpose of magnetic microrobot actuation, soft magnetic material such as Fe, Ni and Co are commonly used in microscale structures. The main reason is their biocompatibility with surface decomposition methods, however Ni and Co are cytotoxic and pure iron can be biodegradable [4]. ORMOCOMP helical swimmers were coated onto a thin layer of Fe (25nm) using electron beam decomposition.

Microrobot Image	Design	Fabrication Method	propulsion method	Citation
	<ul style="list-style-type: none"> • Helical Screw Shape 	<ul style="list-style-type: none"> • Direct Writing (DLW) • Two-photon Polymerization 	<ul style="list-style-type: none"> • Laser RFT 	• [3]
	<ul style="list-style-type: none"> • Helical rigid tail 	<ul style="list-style-type: none"> • Direct Writing (DLW) • Two-photon Polymerization 	<ul style="list-style-type: none"> • Laser RFT 	• [5]
	<ul style="list-style-type: none"> • Planar flexible tail 	<ul style="list-style-type: none"> • The EMA coil system 	<ul style="list-style-type: none"> • SBT RFT 	• [11]
	<ul style="list-style-type: none"> • Cilia 	<ul style="list-style-type: none"> • The EMA coil system 	<ul style="list-style-type: none"> • SBT 	• [11]

Chapter 2: Methods

In this chapter the design of microhelix is described and a few number of design is presented. It followed by introducing the fabrication mechanism, the technology applied to fabricate microstructures and post-processing fabricated microstructures. The simulation is major part of this chapter which is modelling the swimming mechanism of microhelix in high viscous fluid. Three models studied for describing the swimming motion of the microhelix and one model (RFT) is implemented to simulate microhelix with two and six degrees of freedom. The torque driven magnetic field is selected to actuate the microhelix and as a result the relation between the rotational velocity and translational velocity is achieved.

2.1 Microrobot design

For the purpose of this study, the design of microrobots is focused on a helical tail shape with possible propeller head. The helical shape microrobot has generally copied the design of the helical rigid tail flagellum which is a one-dimensional structure. There are other microstructures such as cilia and planar flexible tail flagellum that are copied to build a swimming microrobot. The helical rigid tail flagellum is a preferred design for the micro swimmer as its simplicity makes it feasible to copy in micro scale. In addition, its swimming mechanism is more efficient than other type of microswimmers [5]. Therefore, the key characters of the helix were identified and all the design was based on optimising these characters.

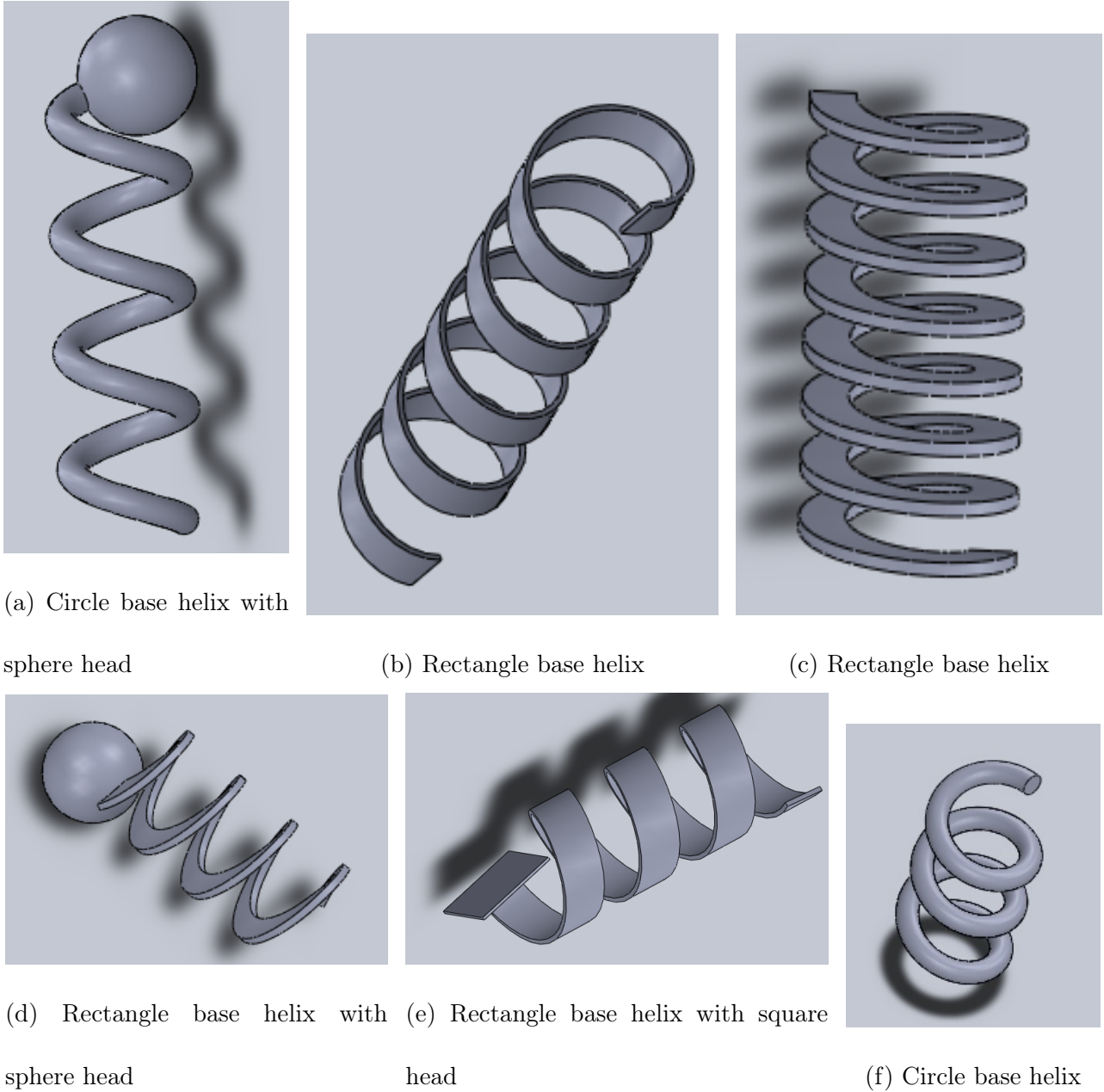


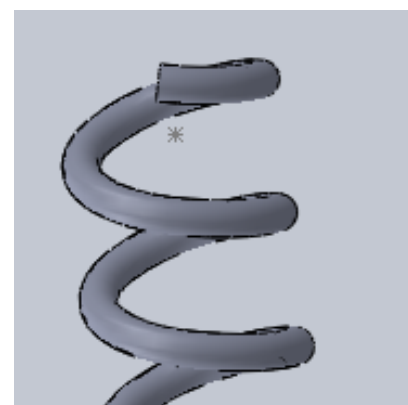
Figure 2.1: (a) Circle base filament helix with a sphere head and three turns. (b) The rectangle base filament helix with larger side of the rectangle was revolved about a spiral path (b) whilst in (c) smaller side of the rectangle revolved about a spiral path. The rectangle base helix can be integrated to sphere head (d) or square head (e).

The figure 2.1 represents the variety of designs that have been undertaken in the design stage of this project. A circle base helix with (2.1a) and without sphere head (2.1f) has been designed. Also their pitch, helical angle and length of the helix were changed to monitor its behaviour during simulation and fabrication process. Two types of rectangle base helix has designed. In the first one, the larger side of the rectangle revolves around a spiral path (2.1b) whilst in the second one the smaller side of the rectangle revolves around the spiral path (2.1c). The former design advantages in the simulation process because its shape produce larger force to propell the microrswimmer. However, the it behave poorly in the fabrication process because it has not provide sufficient surface area to contact with the substrate. Therefore we can't print it vertically. The latter provides strong base for printing vertically but ca't generate sufficient force to move the microswimmer forward. The new design of microhelix which has variable pitch rather than constant pitch is made (??) and fabricated vertically. The advantage of variable pitch design is providing strong base to fabricate it vertically.

2.2 Microrobot fabrication

The main challenge of the fabrication process is not just fabricating the extremely small object. There are number of other factors that need to be considered to select an appropriate approach for fabricating helical shape mincrorobot. An ideal fabrication approach should have control over design parameters and in particular it should be suitable for applying magnetic material for the actuation purpose [5].

The complete fabrication process is summarised in the diagram ???. The process started by importing the structure files into the software called Describe for the pre-processing purpose. The structures file contains all the



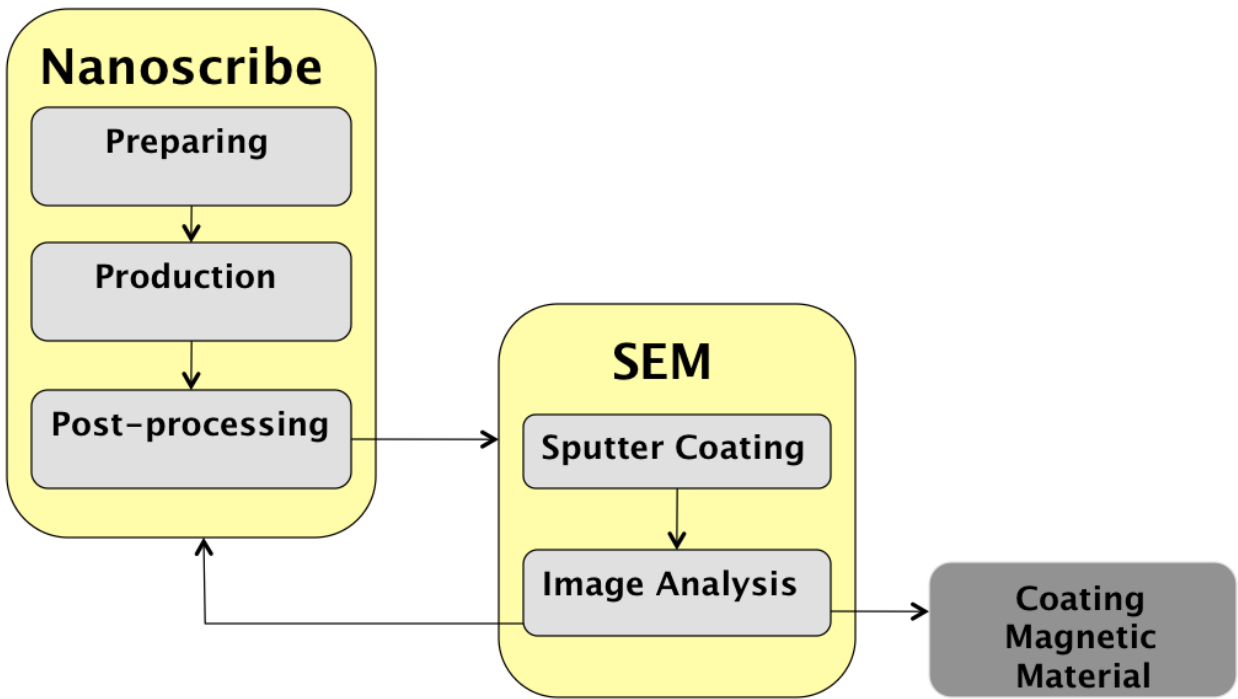


Figure 2.3: Fabrication process overview. The last block of the diagram on the right (dark gray) did not try in this study.

microrobots that is designed by the software called Solid-work. The next stage is writing the structure using nanoscribe facility, which is carried out in the clean room. After the structures printed, they can be seen under the SEM. However, the structure made of polymer and the pictures of non-metal object under the SEM is not perfect. Thus the polymer made microrobot were first coated with a layer of metal (usually gold) and this process is called sputtering coating process. At this stage, the picture of microrobot were analysed under the SEM and if they are satisfactory, they will go to the final stage which is magnetization process. However, we the magnetization stage was not attempted in this project because the aim was to optimise the structures in terms of design and fabrication and there was no plan to run an experiment within the short period of time. The pictures identified as having a problem were sent to the design stage for further optimisation pro-

cess. In the following two sections, we will explain the mechanism of the two photon lithography techniques and SEM in more detail.

2.2.1 Nanoscribe

Nanoscribe is a company providing a sophisticated system and device for true 3D micro and nanofabrication. Their system is based on the laser lithography and it used two-photo polymerization technique for the fabrication. The fabrication device combines two modes for writing; the high-speed galvo-mode and an ultra-precise piezo-mode. The former is for fastest fabrication and it makes the structure in a layer-by-layer process. The latter is mainly for printing arbitrary 3D trajectories [17]. The complete nanoscribe package is made up of three components, Photonic Professional GT, the software and IP Photoresists. Photosensitive material is used in both modes for structuring arbitrary 3D patterns in a high-resolution. The properties of the photosensitive material, the laser power and the size of the spot in the material determined the voxel size. Extremely small voxel size can be achieved when focusing optics is used with a high numerical aperture. The fabrication process in each mode is based on moving the voxel relative to the sample. The galvo mode approach is called Moving-beam Fixed-sample (MBFS) in which the laser beam is scanned and galvanometric mirrors and piezo-actuators will control the vertical movement. However in piezo-mode, piezo actuators move the substrate in all three dimensions to achieve a highly precise focus trajectory. This type of implementation is know as Fixed-beam Moving-sample (FBMS) [17].

The whole process of fabrication is formed of three stages; preparation, production and post-processing. In the first stage, the STereoLithography (stl) file that contains the design of structures will import into the software tool called DeScribe. In this software, each design will go though three steps for fixing the mesh, slicing and hatching. By completing these three steps, the result

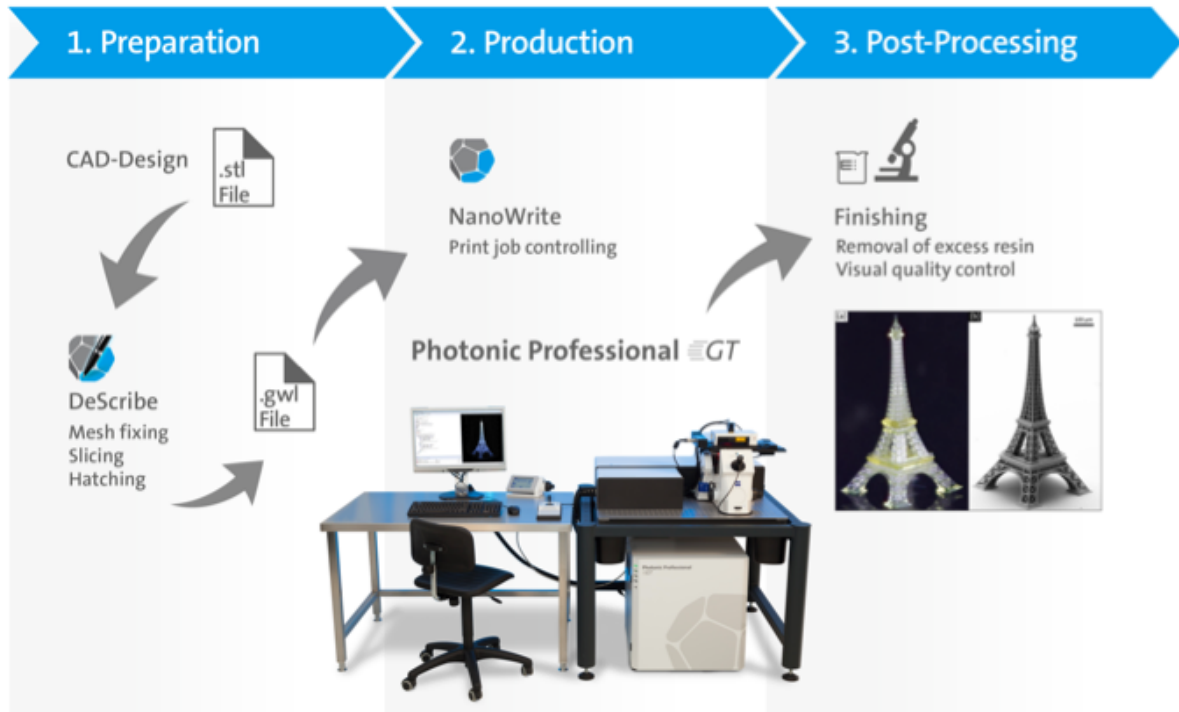
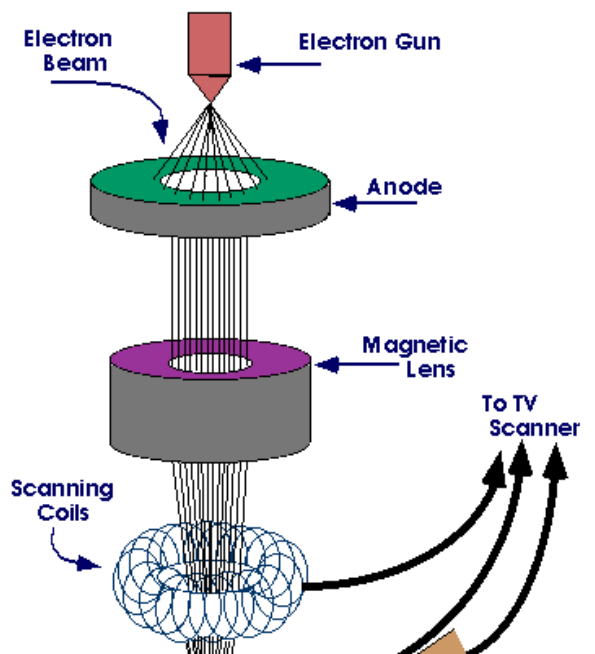


Figure 2.4: nanoscribe workflow. The stages are involved in 3D micro-printing with nanoscribe device is shown in the diagram [17].

will be the General Writing Language (gwl) format file that is ready for the production stage. The production is the stage for controlling the print job that has been done by user-friendly graphical interface software, NanoWrite. This software controls different aspect of the lithography system such as autofocus, exposure dose and substrate positioning. The final stage involves removing the excess resin in order to improve the visual quality [17].

IP Photoresists is a high viscose fluid that comes as part of nanoscribe package. It is used to maximise the performance of the multiphoton polymerization process. It has high mechanical stability and sticks very well to different substrate [17]. A wide range of material with different mechanical, optical or chemical properties can be used for the substrate in di-



rect laser writing. The choice of the substrate material is application dependent. For example in optical applications the transparent material such as glass is more appropriate. In the latter application, the substrate is mainly for supporting to the polymer structures. Also, we can use pre-structured substrates such as transparent micro-fluidic chip so that polymer structure can be printed on the substrate. In that case, the functionality of multiphoton lithography can be improved by combining the mechanical parts with substarte [17].

In this project we used a nanoscribe device to print microswimmers using the galvo-mode of the machine. The whole printing unit is located in the clean room¹. The fabricated structures were observed under the SEM and all the resulting images are presented and discussed in the result 3 and discussion chapters 4 respectively.

2.2.2 Scanning Electron Microscope (SEM)

SEM is a powerful device for obtaining high magnification images to analyse and examine the material or individual features. SEM was invented 50 years ago and is used extensively in diverse scientific fields such as biology, medicine or metallurgy, to name just a few. The SEM can provide images with the high-resolution down to 25 Angstroms.²

SEM generates a range of signals at the surface of solid specimens by using a focused beam of high-

¹Clean room is an environment with controlled concentration of airborne particles to make it suitable for product manufacturing [19].

²1 Angstrom = 1.0×10^{-10} Metres

energy electrons. The process starts with the electron gun producing an electron beam at the top of the microscope which then travels into the microscope. The microscope is placed in the vacuum. The beam is then focused down onto the specimen by passing through the electromagnetic fields and lenses. Once the focused electron beam interacts with the specimen, electrons are revealed from the specimen. At this point, the back-scattered electrons are collected by the detectors and converted into variety of signals. Ultimately, generated signals sent to the screen to form the final image of the specimen[18].

The key advantages of using SEM over traditional microscope is having the large depth of field and the higher resolution. In addition, researchers have more control over the degree of magnification because SEM uses electromagnets[18].

We need to prepare samples before using the SEM because it uses the electron in a vacuum condition. That means the sample should not contain any water as otherwise the water will vaporise in the vacuum. This is a high-vacuum SEM. If we require an image of a wet sample such as biological specimen we can use the low-vacuum SEM. In that case, the specimen chamber contains air that avoid dehydrating of samples. Because the produced images are based on the electron-sample interaction, if the sample is made of non-metal material, the final image is not very clear. Thus, the sample needs to be covered by a metal in order to make it conductive. The process of covering the sample with metal is called sputter coating[18].

sputter coating In the sputter coater, there is small chamber in the vacuum to place the sample in. An electric field and argon gas is used in order to release the electron from the argon and convert it into positively charged atom. Then, argon ions and negatively charged gold foil are attracted to each other and as a result gold atoms fall from the surface of the gold and settle onto the surface of the specimen. Therefore, a thin gold layer covers the surface of the sample and makes it conductive for SEM machine[18].

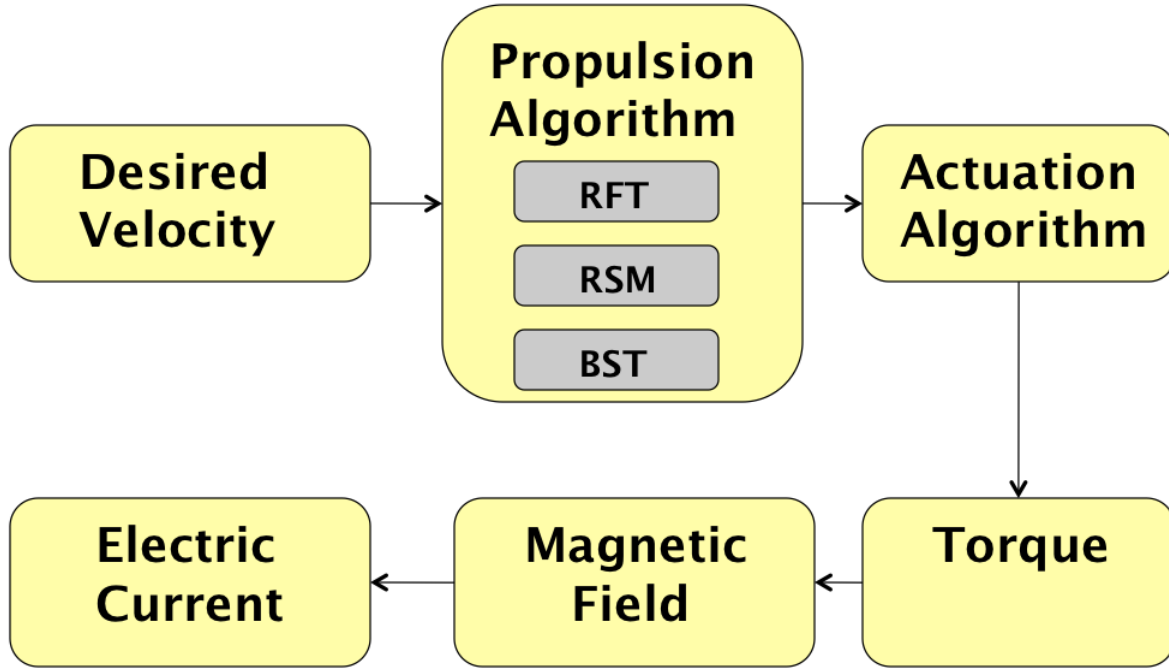


Figure 2.6: Simulation workflow. The microrobot desired velocity is an input of a system. The electric current is required to generate a magnetic field for microrobot actuation is an output.

In this project, the microrobot structure is made of polymer, which we conductive by applying the sputter coating process and then analysing them under SEM. The images of the microrobot structures before and after coating is presented in the result section 3. In the following section, the simulation of microrobot is demonstrated in detail.

2.3 Simulation

The simulation of the microrobot is formed by two main components; helical microrobot propulsion mechanism and actuation method. The complete algorithm that describes the implementation of the simulation system is represented in the diagram 1. In this algorithm, the desired velocity is given to the system and the required electric current to make the dynamic magnetic field will be an output of the system. The pseudocode of the algorithm 1 is provided in more details in each step of the implementation and the complete computation is explained in section 2.3.1.2 and section

2.3.2.

Data: Velocity (\mathbf{V}), RFT, RSM, SBT

while $\mathbf{V} \neq 0$ **do**

Select propulsion method from (RFT, RSM, SBT);

Compute propulsion matrix coefficient (b, c);

Decompose \mathbf{V} to \mathbf{V}_{hor} and \mathbf{V}_{ver} ;

if $\|\mathbf{V}_{hor}\| = 0$ **then**

Rotational velocity $\Omega = \frac{\|\mathbf{V}\| + d_{11}\|\mathbf{f}\|}{e_{11}}$;

Microrobot direction point $\tilde{\mathbf{X}} = -\hat{\mathbf{g}}$;

Go to next step

else

Rotational velocity $\Omega = \frac{\|\tilde{\mathbf{V}}\| \cos(\psi) + d_{11}\|\mathbf{f}\| \cos(\psi - \alpha)}{e_{11}}$;

Microrobot direction point $\tilde{\mathbf{X}} = \frac{\tilde{\mathbf{V}}}{\|\tilde{\mathbf{V}}\|}$;

Go to next step;

end

Compute Torque $\tau = b\mathbf{V} + \Omega c$;

Compute Magnetic field \mathbf{B} from $\tau = \mathbf{V}M \times \mathbf{B}$;

Compute Electric current i from $|\mathbf{B}| = (\frac{b^2}{(b^2 + l^2)^{3/2}})\mu_0 i$

end

Algorithm 1: Simulation algorithm

2.3.1 Modelling helical propulsion

Analysing fluid dynamic phenomena on microorganism is a fundamental approach to model microorganism locomotion [20].

A helical bacterial flagellum can be used as a reference to model a helical microrobot. The essential parameters to model a helix are, helix length (L), pitch (λ), pitch angle (θ), radius (R),

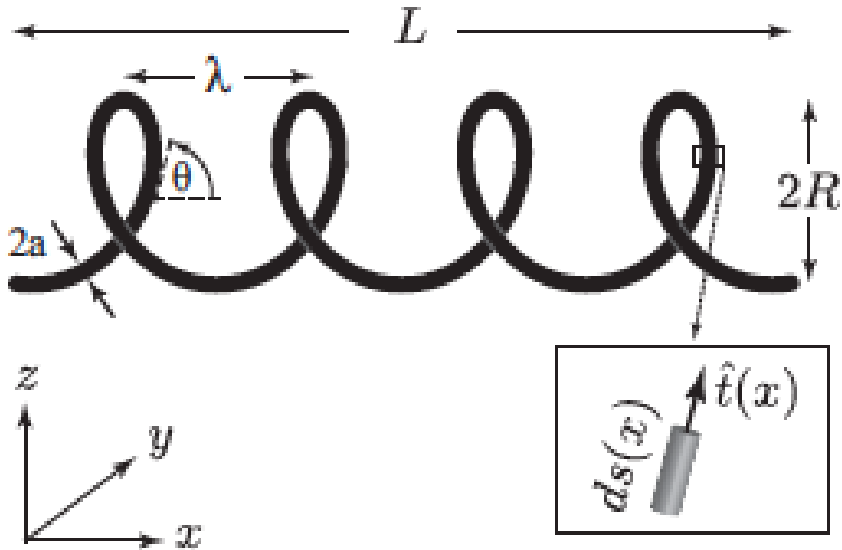


Figure 2.7: The essential helix parameters to design a helical microrobot [8].

filament radius (a) and contour length ($\Lambda = L/\cos \theta$). Figure 2.7 shows the helix parameters evidently [8]. The flagella parameters were measured for several species of bacteria and its result showed the helical pitch is typically ranging between $2R$ and $11R$, ($2R < \lambda < 11R$). Also the helix length (L) varies from 3λ to 11λ , ($3\lambda < L < 11\lambda$).

The flagella rotation at low Reynolds number exerts an axial thrust (F) and torque (T) related to the rotation rate (ω) and flagellum axial velocity (ν). At the same time, fluids was exerted on the force ($-F$) and the torque ($-T$) on the swimming microrobots [14]. The fluid dynamic is governed by the Stokes equations (2.1) in the low Reynolds regime;

$$-\nabla p + \eta \nabla^2 \nu = 0 \quad (2.1)$$

Where η and p are fluid dynamic velocity and pressure respectively. Therefore, thrust (F) and torque (T) are linearly related to the ν and ω as there is no derivation of time in the equations 2.1. These linear relationship can be defined as follow;

$$F = A\nu + B\omega \quad (2.2)$$

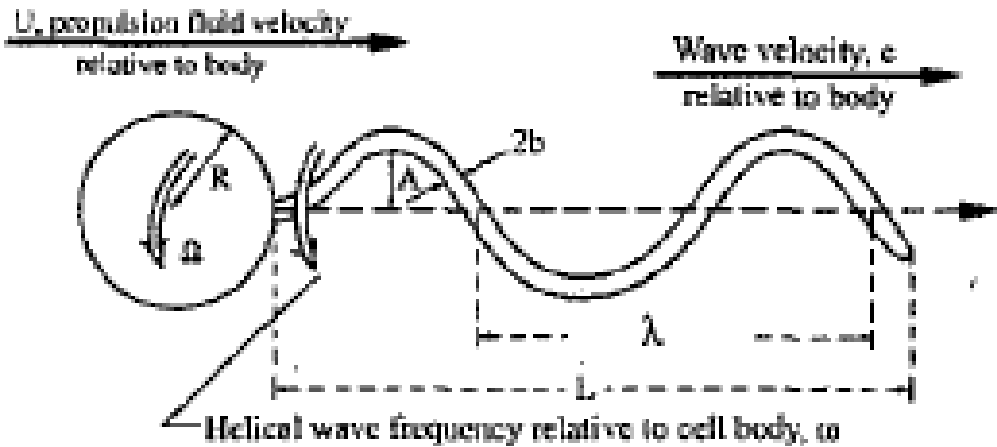


Figure 2.8: Analysis of arbitrary filament motion of microhelix [2].

$$T = C\nu + D\omega \quad (2.3)$$

Therefore, a matrix $\begin{pmatrix} A & B \\ C & D \end{pmatrix}$ defined as propulsion matrix the model to explain the flagella swimming motion described by following equation [8] as mentioned in the literature review earlier;

$$\begin{bmatrix} F \\ T \end{bmatrix} = \begin{bmatrix} A & B \\ C & D \end{bmatrix} \begin{bmatrix} \nu \\ \omega \end{bmatrix}$$

The elements in the symmetric 2×2 matrix (propulsive matrix) in the above equation only depends on flagellum geometry. The propulsive matrix elements can be computed by three methods called; resistive force theory, slender body theory and regularized Stokeslet theory which are described in detail in sections 2.3.1.1, 2.3.1.4 and 2.3.1.3 respectively.

2.3.1.1 Resistive force theory for microrobot with two degrees of freedom

The swimming velocity and efficiency of the microrobot can be predicted by Resistive force theory (RFT) [14]. The force exerted on the fluid by micro swimmer were calculated initially and the micro swimmer will have a net movement if the force is not zero [21]. Furthermore, the swimming

velocity will decrease if the helical body is attached to the inner head. Figure 2.9 shows an arbitrary filament motion which is defined by $s(l, t)$. A direction of the helix velocity (U) is along x-axis and its rotation is symmetric about the x-axis. The following assumption has been made in order to use the RFT.

The geometry of the helix is on the yz-plane and

it always attached to the robot body (can be a sphere). The filament motion is periodic and the filament length is constant at all the time.

Acceleration can be neglected as the system is in the low Re number fluid. Hence, the equations 2.4 and 2.5 will describe the force balance and the moment balance in the x-axis direction. The thrust and torque will be determined by integrating over the first term of the force balance and moment balance equations (2.4 and 2.5) respectively [2].

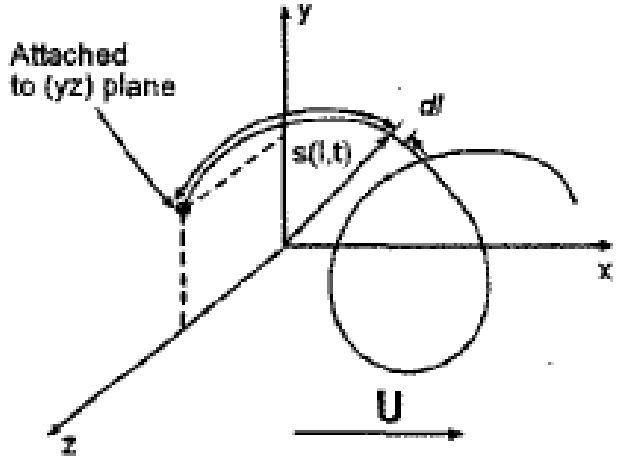


Figure 2.9: A motion of an arbitrary filament [2].

$$\frac{1}{\Delta T} \int_0^{\Delta T} \int_0^L f_x(l, t) \, dl \, dt + C_D U = 0 \quad (2.4)$$

$$\frac{1}{\Delta T} \int_0^{\Delta T} \int_0^L [\mathbf{r} \times \mathbf{f}(l, t)] \cdot \mathbf{e}_1 x \, dl \, dt + C_{D\Omega} \Omega = 0 \quad (2.5)$$

Where ΔT is the time filament motion repeats and integration is taken over the whole length (L) of the helix.

In order to solve the integration problem, the force (f) is required to be defined. Therefore, a new coordination system was introduced and the force vector was defined as a composition of force

per unit length in the normal and tangent directions. The two identical motions are considered for the swimming microrobots are; rotating and translating (assumed in the x-axis direction). Hence, the force balance and moment balance equations are simplified as follows;

$$Nf_xL + C_DU = 0 \quad (2.6)$$

$$Nf_yAL + C_{D\Omega}\Omega = 0 \quad (2.7)$$

Where N and A are number of filaments and helical amplitude of filaments respectively. Also f_x and f_y shows the components of the force vector along x and y directions. In addition, C_D and $C_{D\Omega}$ were computed by equations 2.8 and 2.9 where R is radius of the helix and μ is fluid velocity.

$$C_D = 6\pi\mu R \quad (2.8)$$

$$C_{D\Omega} = 8\pi\mu R^3 \quad (2.9)$$

The f_x and f_y are written as composite of forces in the normal and tangent directions;

$$f_x = f_t \cos \theta - f_n \sin \theta \quad (2.10)$$

$$f_y = f_t \sin \theta + f_n \cos \theta \quad (2.11)$$

$$\tan \theta = \frac{\lambda}{2\pi A} \quad (2.12)$$

$$f_t = -C_t(U \cos \theta - \omega A \sin \theta) \quad (2.13)$$

$$f_n = -C_n(-U \sin \theta - \omega A \cos \theta) \quad (2.14)$$

Where C_t and C_n called resistance coefficients [2];

$$C_t = \frac{2\pi\mu}{\ln\left(\frac{2\lambda}{b}\right) - \frac{1}{2}} \quad (2.15)$$

$$C_n = \frac{4\pi\mu}{\ln\left(\frac{2\lambda}{b}\right) + \frac{1}{2}} \quad (2.16)$$

Microrobot's swimming speed and rotation rate were determined by solving the equations 2.13 and 2.14. Therefore, thrust (F), torque (T) and drag (D) on flagellum can be predict by following equations [8];

$$F = (\Omega R)(C_n - C_t) \sin \theta \cos \theta \frac{L}{\cos \theta} \quad (2.17)$$

$$T = (\Omega R^2)(C_n \cos^2 \theta + C_t \sin^2 \theta) \frac{L}{\cos \theta} \quad (2.18)$$

$$D = U(C_n \sin^2 \theta + C_t \cos^2 \theta) \frac{L}{\cos \theta} \quad (2.19)$$

Finally, the efficiency of the helical swimmers can be computed as follow;

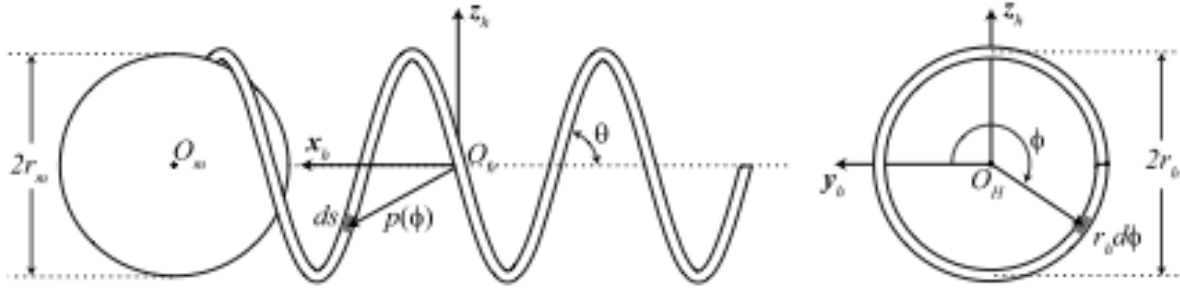


Figure 2.10: Three dimension configuration for the helical microrobot with a magnetic spherical head. The origin of the helix coordinate is denoted with O_h and x_h is the central axis of the helix [7].

$$\text{efficiency} = \frac{FU}{T\omega} \quad (2.20)$$

2.3.1.2 Resistive force theory for six degrees of freedom

The two degrees of freedom microrobot (one dimension model) with RFT was exhibited a successful result [7] for studying the helical microswimmers. However, complex motion of swimming microrobot could not be explained in one dimension model. Therefore, the RFT was needed to be implemented in three dimension model which means defining a microrobot with six degrees of freedom. The microrobot's is used in this model has a helical tail with the sphere head attached to it as shown in 2.10.

The RFT is applied with the assumption that the force and torque is applied on the helical tail and sphear head are independent. Therefore, the force f_h and torque τ_h of the helical tail are obtained by RFT and f_m and τ_m are force and torque applied on the sphear head respectively. The equation 2.98 is the summation of two forces and torques which is the total force and torque.

$$f = f_h + f_m \quad \tau = \tau_h + \tau_m \quad (2.21)$$

According to the RFT the force on the extremely minuscule segment of the helix is defined by the segment velocity and drag forces acts on that segment. First RFT takes the velocity (\mathbf{V}_s) that was applied on the small length of helix and decompounded it into two vectors, one parallel (\mathbf{V}_{\parallel}) and one perpendicular (\mathbf{V}_{\perp}) to that segment. Also, the drag force is acting on the small length decomposed into two vectors; parallel (ξ_{\parallel}) and perpendicular (ξ_{\perp}) to that segment. Therefore, the force is applied on the small segment is formulated as follow;

$$d\mathbf{f}_{\perp} = \xi_{\perp} \mathbf{V}_{\perp} ds \quad (2.22)$$

$$d\mathbf{f}_{\parallel} = \xi_{\parallel} \mathbf{V}_{\parallel} ds \quad (2.23)$$

Where ξ_{\parallel} and ξ_{\perp} are drag coefficients and they have been approximated by a number of scientists empirically. The fluidic force (\mathbf{f}_h) acting on the helix is computed by integrating over these differential forces along the helix length. Because the integration is performed in three dimensions we need to define two separate coordinate frame, one for the given differential segment (frame s) and one for the helix (frame h). The helix pitch angle (θ) and radius (r_h) is used to define the geometry of the helix with the assumption that the central axe of the helix is parallel to the \mathbf{x}_h . Figure 2.10 presents the helix coordinate origin (O_h) with its three axis ($\mathbf{x}_h, \mathbf{y}_h, \mathbf{z}_h$). The helix is represented in a cylindrical coordinate ³

system with the polar angle ϕ . Each vector in the segment frame (s) can be written in the helix frame (h) by applying a rotation matrix as shown in the equation 2.25;

³The cylindrical coordinate is an extention of the polar coordinate to the three dimension space. It defines based on the radius r , the angle θ and the z coordinate such that the following equation are valid

$$x = r \cos \theta \quad y = r \sin \theta \quad z = z \quad (2.24)$$

$${}^h \mathbf{R}_s(\phi) = \mathbf{R}_x(\phi) \mathbf{R}_y(-\theta) \quad (2.25)$$

Where $\mathbf{R}_x(\phi)$ is rotation of a vector in the segment frame (s) with the ϕ angle with respect to the x axis and then will apply $\mathbf{R}_y(-\theta)$ which rotate the result vector with the $(-\theta)$ angle with respect to the y axis. The final result is a vector in the helix (h) frame 2.26.

$${}^h \mathbf{P}(\phi) = \begin{bmatrix} \frac{r}{\tan(\theta)} & r \cos(\phi) & r \sin(\phi) \end{bmatrix} \quad (2.26)$$

Hence, as appears in the equation 2.27 the differential relating velocity to force can be shown with respect to the frame of a random segment along the helix in the segment frame in three dimension.

$${}^s d\mathbf{f}_s = {}^s \boldsymbol{\Xi} {}^s \mathbf{V}_s ds \quad (2.27)$$

$${}^s \boldsymbol{\Xi} = \begin{bmatrix} \xi_{\parallel} & 0 & 0 \\ 0 & \xi_{\perp} & 0 \\ 0 & 0 & \xi_{\perp} \end{bmatrix} \quad (2.28)$$

In the equation 2.27 the force ${}^s \mathbf{f}_s$ and velocity ${}^s \mathbf{V}_s$ of the segment is represented in the segment's own frame. In the segment frame, the x_s axis is assumed to be parallel to that segment and two other axis (y_s, z_s) are perpendicular to that segment as we can see in the 2.28. Hence, the relationship between forces and velocity can be expressed in the helix frame (2.29) by using the drag coefficient unity matrix 2.28.

$${}^h d\mathbf{f}_s = {}^h \boldsymbol{\Xi}(\phi) {}^h \mathbf{V}_s ds \quad (2.29)$$

where

$${}^h\boldsymbol{\Xi}(\phi) = {}^h\mathbf{R}_s(\phi){}^s\boldsymbol{\Xi}{}^s\mathbf{R}_h(\phi) \quad (2.30)$$

The velocity of the small helix segment \mathbf{V}_s is formed of the rotational helix velocity (ω) and its translational velocity (\mathbf{V}). The summation of the two velocities is described in the equations 2.31.

$$\mathbf{V}_s = \mathbf{V} + \boldsymbol{\omega} \times \mathbf{P}(\phi) = \mathbf{V} - \mathbf{P}(\phi) \times \boldsymbol{\omega} \quad (2.31)$$

The equation 2.31 is the velocity of the segment in the segment frame. This equation can be written with respect of the helix frame, as shown below;

$${}^h\mathbf{V}_s = {}^h\mathbf{V} - \Delta\{{}^h\mathbf{P}(\phi)\}^h\boldsymbol{\omega} = {}^h\mathbf{V} + \Delta\{{}^h\mathbf{P}(\phi)\}^{Th}\boldsymbol{\omega} \quad (2.32)$$

where the vector cross product $(\mathbf{P}(\phi) \times \boldsymbol{\omega})$ can be represented in the form of skew-symmetric matrix⁴ $\Delta\{{}^h\mathbf{P}(\phi)\}^h$ and a vector $\boldsymbol{\omega}$:

$$\mathbf{P}(\phi) \times \boldsymbol{\omega} = \Delta\{{}^h\mathbf{P}(\phi)\}^h\boldsymbol{\omega} \quad (2.33)$$

And according to the skew-symmetric matrix property we have:

$$-\Delta\{{}^h\mathbf{P}(\phi)\}^h = \Delta\{{}^h\mathbf{P}(\phi)\}^{Th} \quad (2.34)$$

After substituting 2.32 into 2.29:

⁴In mathematics, a square matrix A is called a skew-symmetric if its transpose is equal to its negative ($A^T = -A$).

$${}^h d\mathbf{f}_s = {}^h \boldsymbol{\Xi}(\phi) {}^h \mathbf{V} ds + {}^h \boldsymbol{\Xi}(\phi) \Delta \{{}^h \mathbf{P}(\phi)\}^{Th} \omega ds \quad (2.35)$$

The equation 2.35 manifests the relationship between differential force and translation and rotation velocity of the small helix segment in the helix frame. Each force is applied on an infinitesimally small section of helix generates a torque around helix centre. As a result the relation between the force and torque at an arbitrary slice of helix (using parameter ϕ) can be represented in the helix frame:

$${}^h d\boldsymbol{\tau}_s = {}^h \mathbf{P}(\phi) \times {}^h d\mathbf{f}_s = \Delta \{{}^h \mathbf{P}(\phi)\} {}^h d\mathbf{f}_s \quad (2.36)$$

Therefore the total fluidic torque and force of the helix can be figured out by integrating the small torques and forces that applied to the extremely small segments of the helix along the helix length:

$$\mathbf{f}_h = \int d\mathbf{f}_s \quad \boldsymbol{\tau}_h = \int d\boldsymbol{\tau}_s \quad (2.37)$$

The final torque and force can be obtained from the equations 2.98 by integrating with respect to the polar angle ϕ . As it been seen in the figure 2.10 the ds can be written with respect to the polar angle ϕ as follow:

$$ds = \frac{r_h d\phi}{\sin(\theta)} \quad (2.38)$$

after substituting the 2.35 into 2.36 and replacing ds with the eqation 2.38 we have the following equations which is integrating with respect with ϕ from $-\pi n$ to πn for an n turn helix;

$$\begin{aligned} {}^h \mathbf{f}_h &= \left(\frac{r_h}{\sin(\theta)} \int_{-\pi n}^{\pi n} {}^h \Xi(\phi) d(\phi) \right) {}^h \mathbf{V} \\ &\quad + \left(\frac{r_h}{\sin(\theta)} \int_{-\pi n}^{\pi n} {}^h \Xi(\phi) \Delta \{{}^h \mathbf{P}(\phi)\}^T d(\phi) \right) {}^h \boldsymbol{\omega} \end{aligned} \quad (2.39)$$

$$\begin{aligned} {}^h \boldsymbol{\tau}_h &= \left(\frac{r_h}{\sin(\theta)} \int_{-\pi n}^{\pi n} \Delta \{{}^h \mathbf{P}(\phi)\} {}^h \Xi(\phi) d(\phi) \right) {}^h \mathbf{V} \\ &\quad + \left(\frac{r_h}{\sin(\theta)} \int_{-\pi n}^{\pi n} \Delta \{{}^h \mathbf{P}(\phi)\} {}^h \Xi(\phi) \Delta \{{}^h \mathbf{P}(\phi)\}^T d(\phi) \right) {}^h \boldsymbol{\omega} \end{aligned} \quad (2.40)$$

Computing all four integrals in the equations 2.39 and 2.40 will result in two equations that is expressed force (${}^h \mathbf{f}_h$) and torque (${}^h \boldsymbol{\tau}_h$) in terms of the angular (${}^h \boldsymbol{\omega}$) and translational velocity (${}^h \mathbf{V}$):

$$\begin{bmatrix} {}^h \mathbf{f}_h \\ {}^h \boldsymbol{\tau}_h \end{bmatrix} = \begin{bmatrix} {}^h \mathbf{A}_h & {}^h \mathbf{B}_h \\ {}^h \mathbf{C}_h & {}^h \mathbf{D}_h \end{bmatrix} \begin{bmatrix} {}^h \mathbf{V}_h \\ {}^h \boldsymbol{\omega} \end{bmatrix}$$

Where ${}^h \mathbf{A}_h$, ${}^h \mathbf{B}_h$ and ${}^h \mathbf{C}_h$ are:

$${}^h \mathbf{A}_h = \begin{bmatrix} a_{h11} & 0 & 0 \\ 0 & a_{h22} & 0 \\ 0 & 0 & a_{h22} \end{bmatrix} \quad (2.41)$$

$${}^h \mathbf{B}_h = \begin{bmatrix} b_{h11} & 0 & b_{h13} \\ 0 & b_{h22} & 0 \\ 0 & 0 & b_{h33} \end{bmatrix} \quad (2.42)$$

$${}^h\mathbf{C}_h = \begin{bmatrix} c_{h11} & 0 & c_{h13} \\ 0 & c_{h22} & 0 \\ c_{h13} & 0 & c_{h33} \end{bmatrix} \quad (2.43)$$

and each matrix element will calculate by following equations:

$$a_{h11} = \frac{2\pi n r_h (\xi_{\parallel} \cos^2(\theta) + \xi_{\perp} \sin^2(\theta))}{\sin(\theta)} \quad (2.44)$$

$$a_{h11} = \frac{\pi n r_h (\xi_{\perp} + \xi_{\perp} \cos^2(\theta) + \xi_{\parallel} \sin^2(\theta))}{\sin(\theta)} \quad (2.45)$$

$$b_{h11} = 2\pi n r_h^2 (\xi_{\parallel} - \xi_{\perp}) \cos(\theta) \quad (2.46)$$

$$a_{h13} = \frac{-2\pi n r_h^2 (\xi_{\parallel} - \xi_{\perp}) \cos(\theta)}{\tan(\theta)} \quad (2.47)$$

$$a_{h22} = \frac{-3\pi n r_h^2 (\xi_{\parallel} - \xi_{\perp}) \cos(\theta)}{2} \quad (2.48)$$

$$a_{h33} = \frac{-\pi n r_h^2 (\xi_{\parallel} - \xi_{\perp}) \cos(\theta)}{2} \quad (2.49)$$

$$c_{h11} = \frac{2\pi n r_h^3 (\xi_{\perp} \cos^2(\theta) + \xi_{\parallel} \sin^2(\theta))}{\sin(\theta)} \quad (2.50)$$

$$c_{h11} = \frac{-2\pi n r_h^3 (\xi_{\perp} \cos^2(\theta) + \xi_{\parallel} \sin^2(\theta))}{\sin(\theta) \tan(\theta)} \quad (2.51)$$

$$\begin{aligned}
c_{h22} = & \frac{2\pi nr_h^3(\xi_{||}\cos^2(\theta) + \xi_{\perp}\sin^2(\theta) - \xi_{\perp}/2)}{\sin(\theta)} \\
& + \frac{\pi nr_h^3(\xi_{||}\cos^2(\theta) - \xi_{\perp}\sin^2(\theta) - \xi_{\perp})}{2\tan^2(\theta)\sin(\theta)} \\
& + \frac{(\pi nr_h)^3(\xi_{||}\cos^2(\theta) - \xi_{\perp}\sin^2(\theta) + \xi_{\perp})}{3\tan^2(\theta)\sin(\theta)} \quad (2.52)
\end{aligned}$$

$$\begin{aligned}
c_{h33} = & \frac{\pi nr_h^3\xi_{\perp}}{\sin(\theta)} - \frac{\pi nr_h^3(\xi_{\perp}\cos^2(\theta) + \xi_{||}\sin^2(\theta) - \xi_{\perp})}{2\tan^2(\theta)\sin(\theta)} \\
& + \frac{(\pi nr_h)^3(\xi_{\perp}\cos^2(\theta) + \xi_{||}\sin^2(\theta) + \xi_{\perp})}{3\tan^2(\theta)\sin(\theta)} \quad (2.53)
\end{aligned}$$

We assumed the fluidic torque and force are applied on microrobot by helical tail is independent from the spherical head. We define a vector \mathbf{K} such that it connects the centre of the helix \mathbf{O}_h to the centre of the spherical magnetic head \mathbf{O}_m as shown in the Figure 2.10. The well-known equations for the rotational and translational drag coefficient of the sphear particle in the stokes flow are [22]:

$$\xi_{vm} = 6\pi\eta r_m \quad \xi_{\omega m} = 8\pi\eta r_m^3 \quad (2.54)$$

Where η is the fluid viscosity and r is the radius of the sphear. A magnet velocity is produced by an arbitrary movement of the microswimmer and can be expressed in the helix frame as the product of the head's velocity and translational drag coefficient:

$${}^h\mathbf{V}_m = {}^h\mathbf{V} + {}^h\boldsymbol{\omega} \times {}^h\mathbf{K} = {}^hV - {}^h\mathbf{K} \times {}^h\boldsymbol{\omega} = {}^h\mathbf{V} + \Delta\{{}^h\mathbf{K}\}^T {}^h\boldsymbol{\omega} \quad (2.55)$$

Also, force on the spherical magnet is the product of the translational and rotational force:

$${}^h\mathbf{f}_m = \xi_{vm} {}^h\mathbf{V} + \xi_{vm} \Delta\{{}^h\mathbf{K}\}^T {}^h\boldsymbol{\omega} \quad (2.56)$$

The force acts at the arm \mathbf{K} and the drag is generated by the rotation of the spherical magnet will cause a drag torque by magnet head:

$${}^h\boldsymbol{\tau}_m = {}^h\mathbf{K} \times {}^h\mathbf{f}_m + \xi_{\omega m} {}^h\boldsymbol{\omega} \quad (2.57)$$

After replacing ${}^h\mathbf{f}_m$ with 2.56 and using screw-symmetric matrix instead of cross-product, the final torque for magnetic head will be:

$${}^h\boldsymbol{\tau}_m = \xi_{vm} \Delta \{{}^h\mathbf{K}\} {}^h\mathbf{V} + (\xi_{vm} \Delta \{{}^h\mathbf{K}\} \Delta \{{}^h\mathbf{K}\}^T + \xi_{\omega m} \mathbf{I}) {}^h\boldsymbol{\omega} \quad (2.58)$$

We can write the equation ?? in terms of matrices;

$${}^h\mathbf{A}_m = \xi_{vm} \mathbf{I} \quad {}^h\mathbf{B}_m = \xi_{vm} \Delta \{{}^h\mathbf{K}\}^T \quad {}^h\mathbf{B}_m = \xi_{vm} \Delta \{{}^h\mathbf{K}\} \Delta \{{}^h\mathbf{K}\}^T + \xi_{\omega m} \mathbf{I} \quad (2.59)$$

Therefore, the total torque (${}^h\boldsymbol{\tau} = {}^h\boldsymbol{\tau}_h + {}^h\boldsymbol{\tau}_m$) and force (${}^h\mathbf{f} = {}^h\mathbf{f}_h + {}^h\mathbf{f}_m$) applied on microswimmer are:

$$\begin{bmatrix} {}^h\mathbf{f} \\ {}^h\boldsymbol{\tau} \end{bmatrix} = \begin{bmatrix} {}^h\mathbf{A} & {}^h\mathbf{B} \\ {}^h\mathbf{B}^T & {}^h\mathbf{C} \end{bmatrix} \begin{bmatrix} {}^h\mathbf{V} \\ {}^h\boldsymbol{\omega} \end{bmatrix}$$

By replacing the matrices with their equivalent;

$$\begin{aligned} \begin{bmatrix} {}^h\mathbf{f} \\ {}^h\boldsymbol{\tau} \end{bmatrix} &= \begin{bmatrix} {}^h\mathbf{A}_h + {}^h\mathbf{A}_m & {}^h\mathbf{B}_h + {}^h\mathbf{B}_m \\ ({}^h\mathbf{B}_h + {}^h\mathbf{B}_m)^T & {}^h\mathbf{C}_h + {}^h\mathbf{C}_m \end{bmatrix} \begin{bmatrix} {}^h\mathbf{V} \\ {}^h\boldsymbol{\omega} \end{bmatrix} \\ {}^h\mathbf{A} &= \begin{bmatrix} a_{11} & 0 & 0 \\ 0 & a_{22} & 0 \\ 0 & 0 & a_{22} \end{bmatrix} = \begin{bmatrix} a_{h11} + \xi_{vm} & 0 & 0 \\ 0 & a_{h22} + \xi_{vm} & 0 \\ 0 & 0 & a_{h22} + \xi_{vm} \end{bmatrix} \end{aligned} \quad (2.60)$$

$${}^h\mathbf{B} = \begin{bmatrix} b_{11} & 0 & b_{13} \\ 0 & b_{22} & b_{23} \\ 0 & -b_{23} & b_{33} \end{bmatrix} = \begin{bmatrix} b_{h11} & 0 & b_{h13} \\ 0 & b_{h22} & \xi_{vm}|\mathbf{K}| \\ 0 & -\xi_{vm}|\mathbf{K}| & b_{h33} \end{bmatrix} \quad (2.61)$$

$${}^h\mathbf{C} = \begin{bmatrix} c_{11} & 0 & c_{h13} \\ 0 & c_{22} & 0 \\ c_{h13} & 0 & c_{33} \end{bmatrix} = \begin{bmatrix} c_{h11} + \xi_{\omega m} & 0 & c_{h13} \\ 0 & c_{h22} + \xi_{vm}|\mathbf{K}|^2 + \xi_{\omega m} & 0 \\ c_{h13} & 0 & c_{h33} + \xi_{vm}|\mathbf{K}|^2 + \xi_{\omega m} \end{bmatrix} \quad (2.62)$$

Hence, the total nonfluidic force (\mathbf{f}) which produced as a result of gravity and total nonfluidic torque ($\boldsymbol{\tau}$) generated by magnetic field.

2.3.1.3 Regularized Stokeslet method

A regularization parameter can be used as a proxy for the body radius to minimise numerical errors in modelling a flagellum as a one dimensional filament in a low Reynolds [20]. number fluids. The Regularized Stokeslet method (RSM) is one of the approach to solve the zero Reynolds number linear ‘Stokes flow’ equations;

$$\left. \begin{array}{l} 0 = -\nabla p + \mu \nabla^2 u + f \\ 0 = \nabla \cdot u \end{array} \right\} \text{Stokes flow equations} \quad (2.63)$$

where u (velocity), p (pressure), μ (kinematic viscosity), and f (force) are measured per unit volume. The singular ‘Stokeslet’ solution for the equations 2.63 corresponds to the purely viscous component (point force) of the flow, which was determined by moving sphere. The ‘Stokeslet’ solution for unit force acts in the j -direction and concentrated at ξ , where f is;

$$f(x) = \delta(x - \xi)e_j \quad (2.64)$$

$\delta(\mathbf{x} - \boldsymbol{\xi})$ is called Dirac delta distribution. The velocity in the i -direction driven by this force is defined as follow;

$$S_{ij}(\mathbf{x}, \boldsymbol{\xi}) = \left(\frac{\delta_{ij}}{r} + \frac{r_i r_j}{r^3} \right) \quad (2.65)$$

Where δ_{ij} denotes Kronecker delta tensor, $r_i = x_i - \xi_i$ and $r^2 = |\mathbf{x} - \boldsymbol{\xi}|^2 = r_1^2 + r_2^2 + r_3^2$. The flow concentrates at point $\boldsymbol{\xi}$ by the force \mathbf{F} where $\mathbf{f}(\mathbf{x}) = \delta(\mathbf{x} - \boldsymbol{\xi})\mathbf{F}$. The solution is given by finding the velocity $u_i(\mathbf{x})$;

$$u_i(x) = \left(\frac{1}{8\pi\mu} \right) S_{ij}(\mathbf{x}, \boldsymbol{\xi}) F_j \quad (2.66)$$

The RFT and SBT for modelling of flagellum driven flow were formed on the base of the Stokeslet [20]. These methods solved the three dimentinal flow problem with flexible boundaries without using direct computation for the differential equations. Therefore, the provided solutions are extremely efficient in terms of computational costs. The fluid velocity was modeled by the following equation;

$$\mathbf{u}(\mathbf{x}) = \left(\frac{1}{8\pi\mu} \right) \int_S \mathbf{f}(\boldsymbol{\xi}) \cdot \mathbf{S}(\mathbf{x}, \boldsymbol{\xi}) dS_\xi \quad (2.67)$$

Where S is a collection of lines or surfaces of flagella, $\mathbf{f}(\boldsymbol{\xi})$ shows force per unit length or area. $\mathbf{f}(\boldsymbol{\xi})dS_\xi$ denotes the force flagella body exerted on the fluid and $-\mathbf{f}(\boldsymbol{\xi})dS_\xi$ is the force fluid applies to the body. The flagella is represented by equation 2.67 with the boundary S and parameter $\boldsymbol{\xi}(s)$ where $0 < s < 1$ is scaled arclength parameter. However, the flow field at any point $\mathbf{x} = \boldsymbol{\xi}(s)$ is sigular and the collection of points on the surface of the filament are required to calculate the force per unit length. The collection of points were replaced on a small distance from the centreline;

$$\mathbf{X}(\mathbf{s}_q) = \boldsymbol{\xi}(s_q) + a(s_q)\mathbf{n}(s_q) \quad (2.68)$$

where $a(s_q)$ is a radius of slender body and $\mathbf{n}(s_q)$ is a unit normal vector. Point distributions of Stokeslets at any point $x = \boldsymbol{\xi}_q$ and line distribution inside the notional surface of the flagella are both singular. However, surface distributions of Stokeslets do not result in singular velocity but still requires attentive numerical implementations [20]. The ‘regularized Stokeslet’ introduced an exact solution for the equations ?? to overcome these issues. This method used a cut off function (ψ) with a regularization parameter (ϵ) to smooth point forces such that $\int_{R^3} \psi_\epsilon(\mathbf{x}) dV_x = 1$.

$$\left. \begin{array}{l} 0 = -\nabla p + \mu \nabla^2 \mathbf{u} + \mathbf{f} \psi_\epsilon(\mathbf{x} - \boldsymbol{\xi}), \\ 0 = \nabla \cdot \mathbf{u} \end{array} \right\} \text{Stokes flow equations with regularization parameter} \quad (2.69)$$

In RSM method, with a assumption of $\psi_\epsilon(\mathbf{x} - \boldsymbol{\xi}) := 15\epsilon^4 / 8\pi\mu r_\epsilon^7$ and $r_\epsilon = \sqrt{r^2 + \epsilon^2}$ the regularized Stokeslet velocity tensor measured by the the following:

$$S_{ij}^\epsilon(\mathbf{x}, \boldsymbol{\xi}) = \frac{\delta_{ij}(r^2 + 2\epsilon^2) + r_i r_j}{r_\epsilon^3} \quad (2.70)$$

Therefore the boundary for intergal equation (2.71) is defined and the fluid velocity at location x is;

$$\mathbf{u}(\mathbf{x}) = \left(\frac{1}{8\pi\mu} \right) \int_S \mathbf{f}(\boldsymbol{\xi}) \cdot S^\epsilon(\mathbf{x}, \boldsymbol{\xi}) dS_\xi \quad (2.71)$$

Where $\mathbf{f}(\boldsymbol{\xi})$ denotes a fluidic force per unit area or length depends on $\boldsymbol{\xi}$. $\boldsymbol{\xi}$ could be on a line or on a surface, in both cases for $\mathbf{x} = \boldsymbol{\xi}$ kernel is regular. This is a significant advantage of RSM to model swimming motion of microhelix in a high viscose fluid environment.

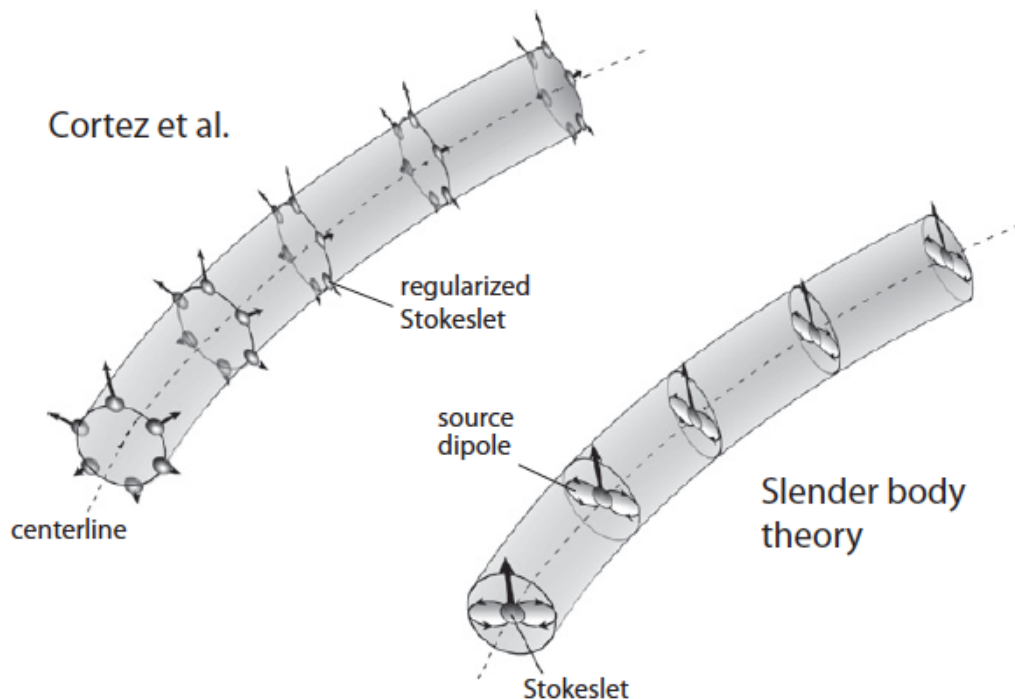


Figure 2.11: RSM and SBT. In RSM the surface of helix filament is separated by cross-sectional segmentation and each surface represents by Stokeslets (left image). In SBT, the Stokeslets are arranged along the central filament line (right image) [8].

2.3.1.4 Slender body theory

Slender body theory represents the helix body with an arrangement of doublets and Stokeslets along the filament central line (Figure 2.11). This theory represented by Lighthill for the first time and was followed by Johnson with some modification. According to Lighthill there is some distance q from any given point on the helix body such that q is between the radius of the filament a and helix pitch λ . The dipoles fallen within this distance are important in determining the flow at the given point. He proved for the induced fluid flow on the given segment the sum of near-field and far-field solutions could be made independent of any distance (q) by defining the dipoles as follow;

$$-\frac{a^2 \mathbf{f}_\perp(s)}{4\mu} \quad (2.72)$$

Where s is a location along the central axis of the filament and $\mathbf{f}_\perp(s)$ is Stokeslets strength's component which is perpendicular to the filament central axis. Therefore the sum of dipole and Stokeslets define the flow induced by each segment of the helix body. As a result there is a relation between the local velocity of a segment on the s location and the force per unit length;

$$\mathbf{u}(s) = -\frac{a^2 \mathbf{f}_\perp(s)}{4\mu} + \int_{|\mathbf{r}_0(s',s)|>\delta} \mathbf{f}(s').J(\mathbf{r}_0) ds' \quad (2.73)$$

Where \mathbf{r}_0 is the vector from the point s on the central axis to the point s' and δ is a natural cutoff ($\delta = \frac{a\sqrt{e}}{2}$). For the spatial location r Oseen tensor J is;

$$J(\mathbf{r}) \equiv \frac{1}{8\pi\mu} \left(\frac{\mathbf{I}}{|\mathbf{r}|} + \frac{\mathbf{r}\mathbf{r}^T}{|\mathbf{r}|^3} \right) \quad (2.74)$$

The thrust, torque and drag of the helical microswimmer can be obtained by applying rectangular rule of numerical integration and as a result we have;

$$J(\mathbf{r}) \equiv \frac{1}{8\pi\mu} \left(\frac{I}{|\mathbf{r}|} + \frac{\mathbf{r}\mathbf{r}^T}{|\mathbf{r}|^3} \right) \quad (2.75)$$

We need to parameterize spatial locations, so we define helical phase $\phi \equiv ks \cos(\theta)$ where $k = 2\pi/\lambda$ and $\mathbf{r} = R(\phi \cot(\theta), \cos(\phi), \sin(\phi))$. Therefore, equation 2.73 is converted to following equation;

$$\mathbf{u}_n = \frac{(I - \hat{t}_n \hat{t}_n + D_n) \cdot \mathbf{f}_n}{4\pi\mu} + \frac{\mathbf{R} \Delta\phi \csc(\theta)}{8\pi\mu} \sum_{m \neq n} \frac{I + \hat{r}_{nm} \hat{r}_{nm}}{r_{nm}} \cdot \mathbf{f}_m + \Lambda(\Delta\phi) \quad (2.76)$$

Where $m, n = 1, 2, \dots, N$ and $\hat{t}_n = (\cos(\theta), -\sin(\theta) \sin(\phi_n), \sin(\theta) \cos(\phi_n))$. The position vector between spatial location is $\mathbf{r}_{nm} = \mathbf{r}(\phi_n) - \mathbf{r}(\phi_m)$.

The components of the velocity \mathbf{u}_n that are invariant alongside the helix can be obtained by integrating over the eqation 2.76 and using the frame rotated with the helical phase. Then we can find the linear mapping between force and velocity per unit length and calculate the rotational and translation velocity to find the force, torque and drag.

The first part of the equation 2.76 is called tensor D_n and it shows the helical segments that are centred at \mathbf{r} . D_n can be expressed in the form of following integral;

$$D_n = 1/2 \int_{|\mathbf{r}-\mathbf{r}_n| \in (\delta, \delta')} ds(\phi) \left(\frac{I}{|\mathbf{r}-\mathbf{r}_n|} + \frac{(\mathbf{r}-\mathbf{r}_m)(\mathbf{r}-\mathbf{r}_m)}{|\mathbf{r}-\mathbf{r}_n|^3} \right) \cdot \chi_z(\phi - \phi_n) \quad (2.77)$$

Where the rotation matrix χ_z is defined as;

$$\chi_z = \begin{bmatrix} \cos(\phi) & -\sin(\phi) & 0 \\ \sin(\phi) & \cos(\phi) & 0 \\ 0 & 0 & 1 \end{bmatrix} \quad (2.78)$$

We define new vectors for force and velocity to simplify the calculation;

$$\mathbf{u}_n' = \chi_z(-\phi_n) \cdot \mathbf{u} \quad (2.79)$$

$$\mathbf{f}_n' = \chi_z(-\phi_n) \cdot \mathbf{f} \quad (2.80)$$

Therefore, the velocity \mathbf{u}_n' is invariant to the filament and the rotational and translational velocity of the helix can be written as;

$$\mathbf{u}_n' = (0, \boldsymbol{\Omega} \mathbf{R}, \mathbf{U})^T \quad (2.81)$$

And the force;

$$\sum_{i=1} \mathbf{f}' \mathbf{R} \Delta \phi \csc \theta = (0, \mathbf{T}/\mathbf{R}, \mathbf{F}_x)^T \quad (2.82)$$

Therefore, SBT can be expressed as;

$$\begin{aligned} \mathbf{u}_n' &= \frac{(I - \hat{t}_n \hat{t}_n + D_n) \cdot \mathbf{f}_n}{4\pi\mu} \\ &+ \frac{\mathbf{R} \Delta \phi \csc(\theta)}{8\pi\mu} \sum_{m \neq n} \frac{\chi_z(\phi_m - \phi_n) + \chi_z(-\phi_n) \cdot \hat{r}_{nm} \hat{r}_{nm} \cdot \chi_z(-\phi_n)}{r_{nm}} \cdot \mathbf{f}_m' \\ &+ \Lambda(\Delta\phi) \end{aligned} \quad (2.83)$$

Where both \hat{t}' and D_n' are invariant to the helical filament,

$$\hat{t}' = (0, \sin \theta, \cos \theta) \quad (2.84)$$

and

$$\int_{k\delta \cos \theta}^{k\delta' \cos \theta} d\phi \frac{1}{\phi} (I + \begin{pmatrix} 0 & 0 & 0 \\ 0 & \sin^2 \theta & \sin \theta \cos \theta \\ 0 & \sin \theta \cos \theta & \cos^2 \theta \end{pmatrix}) = \ln\left(\frac{\delta'}{\delta}\right)(I + \hat{t}'\hat{t}') \quad (2.85)$$

So we obtained the mapping between the force and velocity;

$$\begin{pmatrix} \mathbf{u}_1' \\ \mathbf{u}_2' \\ \vdots \\ \mathbf{u}_N' \end{pmatrix} = \Delta \cdot \begin{pmatrix} \mathbf{f}_1' \\ \mathbf{f}_2' \\ \vdots \\ \mathbf{f}_N' \end{pmatrix} \quad (2.86)$$

For the velocity $\mathbf{u}_n' = \mathbf{u}_0 = (0, \Omega \mathbf{R}, \mathbf{U})^T$ we have;

$$\begin{pmatrix} \mathbf{f}_1' \\ \mathbf{f}_2' \\ \vdots \\ \mathbf{f}_N' \end{pmatrix} = \Delta^{-1} \cdot \begin{pmatrix} \mathbf{u}_0 \\ \mathbf{u}_0 \\ \vdots \\ \mathbf{u}_0 \end{pmatrix} \quad (2.87)$$

Finally, the fluidic force and torque are;

$$(0, \frac{T}{R}, F_x)^T = \sum_{i=1}^N \mathbf{f}' \mathbf{R} \Delta \phi \csc \theta \quad (2.88)$$

2.3.2 Microrobot actuation

In this section the aim is to develop an algorithm for the microrobot velocity control. To achieve this aim, we need to figure out the direction that microrobot points out (\mathbf{X}_h) and then its rotational speed (Ω) to obtain a desired velocity [7]. In this algorithm, the only nonfluidic force is applied on the microrobot is its weight which is expressed as $m\mathbf{g}$. The mass of the microrobot is m and the

vector \mathbf{g} shows the acceleration gravity. The direction of the gravity is downward and represented by $\hat{\mathbf{g}} = \mathbf{g}/\|\mathbf{g}\|$.

Flowchart for Algorithm of the actuation method

Previous research on controlling microswimmers's speed is evident that there is a lack of control if commanding microrobot with too rapid maneuvers [24] [25]. Therefore, in this work we assumed microswimmers can turn continuously to the aimed direction in such a way that the temporary behaviour is ignored. We define $\tilde{\mathbf{X}}$ as the axis magnetic field should always be perpendicular to it. If the microrobot coordinate frame is aligned with the stationary world frame then there it does not need to convert vectors between these two frames. From the helical propulsion equation system, we specifically considered the first equation which is the relationship between non-fluidic force, angular and translational velocity of the microswimmer.

$${}^h \mathbf{f} = {}^h \mathbf{A} {}^h \mathbf{V} + {}^h \mathbf{B} {}^h \boldsymbol{\omega} \quad (2.89)$$

The matrix ${}^h \mathbf{A}$ is invertible, thus the desired velocity can be obtained from the equation 2.89;

$${}^h \mathbf{V} = ({}^h \mathbf{A}^{-1}) {}^h \mathbf{f} + (-{}^h \mathbf{A}^{-1} {}^h \mathbf{B}) {}^h \boldsymbol{\omega} = {}^h \mathbf{D} {}^h \mathbf{f} + {}^h \mathbf{E} {}^h \boldsymbol{\omega} \quad (2.90)$$

$${}^h \mathbf{D}_h = \begin{bmatrix} d_{11} & 0 & 0 \\ 0 & d_{22} & 0 \\ 0 & 0 & d_{22} \end{bmatrix} \quad (2.91)$$

$${}^h \mathbf{E}_h = \begin{bmatrix} e_{11} & 0 & 0 \\ 0 & e_{22} & 0 \\ 0 & 0 & e_{22} \end{bmatrix} \quad (2.92)$$

The equations 2.90, 2.91, 2.92 are in the helix frame and can be converted to the world frame by applying relation matrix ${}^w\mathbf{R}_h$ on the equation 2.90;

$${}^w\mathbf{R}_h{}^h\mathbf{V} = {}^w\mathbf{R}_h{}^h\mathbf{D}^h\mathbf{f} + {}^w\mathbf{R}_h{}^h\mathbf{E}^h\boldsymbol{\omega} \quad (2.93)$$

$${}^w\mathbf{V} = {}^w\mathbf{E}^w\boldsymbol{\omega} + {}^w\mathbf{D}^w\mathbf{f} \quad (2.94)$$

Then by applying the similar transformation to other component 2.91, 2.92;

$${}^w\mathbf{V} = {}^w\mathbf{R}_h{}^h\mathbf{V} \quad {}^w\mathbf{f} = {}^w\mathbf{R}_h{}^h\mathbf{f} \quad {}^w\mathbf{D} = {}^w\mathbf{R}_h{}^h\mathbf{D}^h\mathbf{R}_w \quad {}^w\mathbf{E} = {}^w\mathbf{R}_h{}^h\mathbf{E}^h\mathbf{R}_w \quad (2.95)$$

To obtain ${}^h\mathbf{R}_w$ the orientation of the microrobot needs to be detected whilst it is rotating during propulsion around the axis which is difficult. For that reason, the equation 2.94 is expressed in such way that does not need to know the microrobot orientation whilst rotating about its central axis. Since the microrobot is torque driven and the only nonfoluidic force is involved in equation 2.89 is its weight ($m\mathbf{g}$). The velocity of microrobot can be decomposed to vertical and horizontal components:

$$\mathbf{V}_{ver} = (\mathbf{V} \cdot \hat{\mathbf{g}}) \hat{\mathbf{g}} \quad (2.96)$$

$$\mathbf{V}_{hor} = \mathbf{V} - \mathbf{V}_{ver} \quad (2.97)$$

Two options can be considered for the $\|\mathbf{V}_{hor}\|$:

$$\|\mathbf{V}_{hor}\| = 0 \quad , \quad \|\mathbf{V}_{hor}\| \neq 0 \quad (2.98)$$

The first option is a trivial case, because when the microrobot is being commanded with $\|\mathbf{V}_{hor}\| = 0$, that means the microrobot can only swim vertically in either direction according to the equation 2.97. This is the special case when the six degrees of freedom microrobot will effectively become the microrobot with two degrees of freedom which is pointing in the direction of the gravity acceleration and its angular velocity can be found directly from the equation 2.94:

$$\boldsymbol{\Omega} = \frac{\|\mathbf{V}\| + d_{11}\|\mathbf{f}\|}{e_{11}} , \quad \tilde{\mathbf{X}} = -\hat{\mathbf{g}} \quad (2.99)$$

The second option $\|\mathbf{V}_{hor}\| \neq 0$ is more challenging, because it requires setting the coordinate frame for microrobot which does not rotate when it is rotating around the central axis. The ideal coordinate frame can be constructed by using $\hat{\mathbf{g}}$ and based on the eigenvectors⁵ of ${}^w\mathbf{D}$ or ${}^w\mathbf{E}$. This coordinate system is denoted by p and can be defined as :

$$\mathbf{x}_p = \frac{(\mathbf{x}_h \cdot \mathbf{V}) \mathbf{x}_h}{|\mathbf{x}_h \cdot \mathbf{V}|} \quad (2.100)$$

$$\mathbf{y}_p = \frac{(\mathbf{x}_p \times \mathbf{g})}{\|\mathbf{x}_p \times \mathbf{g}\|} \quad (2.101)$$

$$\mathbf{z}_p = \mathbf{x}_p \times \mathbf{y}_p \quad (2.102)$$

The new (principle) coordinate system will solve the problem because it is invariant to the rotation of the microswimmer around its central axis. Therefore, the equation 2.94 can be expressed in terms of the principle coordinate frame. In the following paragraph, we first configure the representation for the first component (${}^w\mathbf{E} {}^w\boldsymbol{\omega}$) of the equation 2.94 and followed by a similar process on the

⁵If we have a set of data point, the set can be deconstructed into eigenvector and eigenvalue where eigenvector is the direction that data spread out and eigenvalue is the variance of the data in that direction. The principle component is the eigen vector with the largest eigenvalue [26].

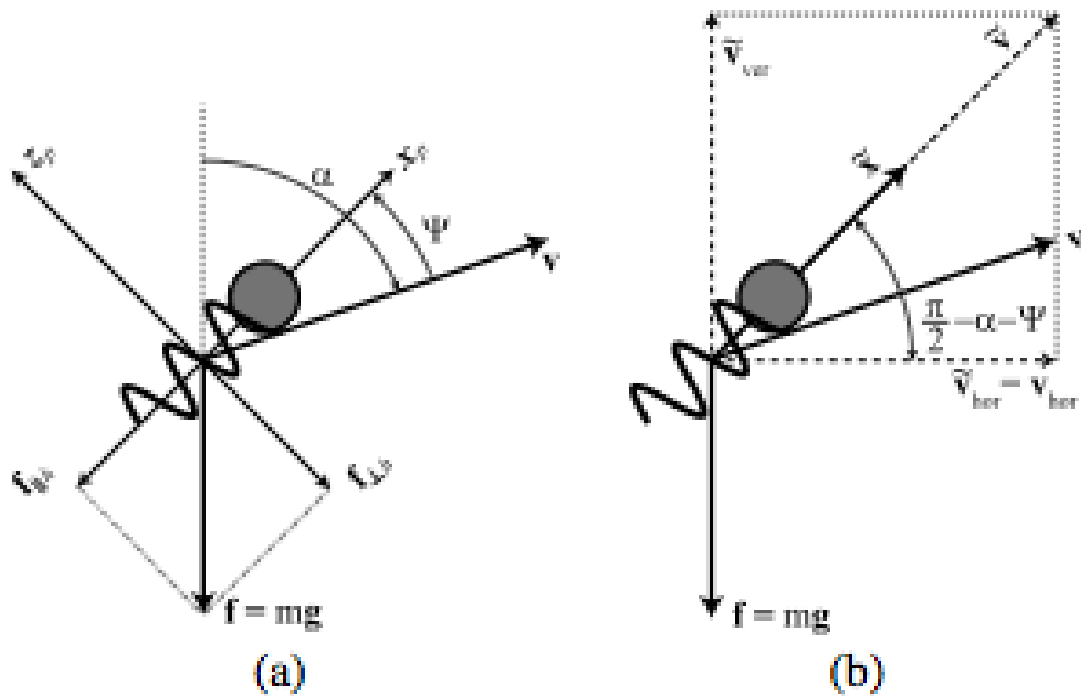


Figure 2.12: (a) The principle coordinate frame based on the gravity and principle components of the matrices in equations 2.92 and 2.91. (b) Construction details of direction of the microswimmer ($\tilde{\mathbf{X}}$) [7].

second component (${}^w\mathbf{D}{}^w\mathbf{f}$). The final result will express the desired velocity vector in terms of the principal coordinate system.

It is assumed that the microrobot is at steady state, that means ${}^w\boldsymbol{\omega} = \Omega {}^w\tilde{\mathbf{x}} = \Omega {}^w\mathbf{x}_p$, also we know two vectors ${}^w\mathbf{x}_p$ and ${}^w\mathbf{x}_h$ are parallel. It has been proved that ${}^h\mathbf{x}_h$ and e_{11} are eigenvector and eigenvalue of matrix ${}^h\mathbf{E}$ respectively [7]. The transformation matrix ${}^w\mathbf{R}_h$ will not affect the eigenvalue (e_{11}) but it will rotate the eigenvector (${}^h\mathbf{x}_h$) from the helix coordinate frame to the global frame (w). As a result (e_{11}) and (${}^w\mathbf{x}_p$) are the eigenvalue and eigenvector in the world coordinate system respectively. By considering the vectors ${}^w\mathbf{x}_p$ and ${}^h\mathbf{x}_p$ are parallel and definition of eigenvalue and eigenvector⁶ the first component of the desired velocity (${}^w\mathbf{E}{}^w\boldsymbol{\omega}$) can be represented in the principle coordinate system as follow:

$${}^w\mathbf{E}{}^w\boldsymbol{\omega} = {}^w\mathbf{E}\Omega {}^w\mathbf{x}_p = e_{11}\Omega {}^w\mathbf{x}_p \quad (2.103)$$

The similar reasoning has been used to represent the second component (${}^w\mathbf{D}{}^w\mathbf{f}$) of the velocity equation (2.94) in terms of the principle coordinate system. In this case, d_{11} and d_{22} are eigenvalues of the matrix ${}^h\mathbf{D}$ such that ${}^h\mathbf{x}_h$ is the eigenvector corresponding to the d_{11} and d_{22} is associated with an eigenspace⁷ spanned by $\{{}^h\mathbf{y}_h, {}^h\mathbf{z}_h\}$. Again, the eigenvalues and eigenspace will remain unaffected under transformation matrix. Thus, the eigenvalue d_{11} is corresponding to the ${}^w\mathbf{x}_h$ and the eigenvalue d_{22} is related to the vector in the subspace $\{{}^w\mathbf{y}_h, {}^w\mathbf{z}_h\}$. In addition, the force vector can be decomposed into two vectors; one parallel to the central axis of helix and the other perpendicular to that axis (${}^w\mathbf{x}_h$):

⁶Assume A is a square matrix $n \times n$, we call λ an eigenvalue of matrix A if the non-zero vector \mathbf{V} exists such that $A\mathbf{V} = \lambda\mathbf{V}$. The vector V is called eigenvector corresponding to eigenvalue λ . [27].

⁷Let A be a $n \times n$ square matrix with an eigenvalue λ . Then the union of all eigenvectors associated with the eigenvalue λ and vector zero is a subspace of \Re^3 which is called the eigenspace for the eigenvalue λ . [28].

$${}^w \mathbf{f} = ((\mathbf{f} \cdot \mathbf{x}_h) {}^w \mathbf{x}_h) + ((\mathbf{f} \cdot \mathbf{y}_h) {}^w \mathbf{y}_h + (\mathbf{f} \cdot \mathbf{z}_h) {}^w \mathbf{z}_h) = {}^w \mathbf{f}_{\parallel h} + {}^w \mathbf{f}_{\perp h} \quad (2.104)$$

If ${}^w \mathbf{f}_{\perp h}$ does not change then both ${}^w \mathbf{f}$ and ${}^w \mathbf{f}_{\parallel h}$ will not change if the microrobot rotate around its central axis. In addition, ${}^w \mathbf{y}_p$ and ${}^w \mathbf{z}_p$ are in the eigenspace formed by $\{{}^w \mathbf{y}_h, {}^w \mathbf{z}_h\}$. As a result, ${}^w \mathbf{f}_{\perp h}$ can be written in the principle coordinate frame as a linear combinations of two vectors ${}^w \mathbf{z}_p$ and ${}^w \mathbf{y}_p$. Because d_{22} is the corresponding eigenvalue of any vector in the span of the $\{{}^w \mathbf{y}_h, {}^w \mathbf{z}_h\}$, so it will be the eigenvalue associated with ${}^w \mathbf{f}_{\perp h}$. Using the fact that d_{11} is the eigenvalue corresponding to ${}^w \mathbf{f}_{\parallel h}$ and implying the transformation matrix we can write the force based on the principle component axis:

$$\begin{aligned} {}^w \mathbf{D} {}^w \mathbf{f} &= {}^w \mathbf{D} {}^w \mathbf{f}_{\parallel h} + {}^w \mathbf{D} {}^w \mathbf{f}_{\perp h} = d_{11} {}^w \mathbf{f}_{\parallel h} + d_{22} {}^w \mathbf{f}_{\perp h} \\ &= d_{11} (\mathbf{f} \cdot \mathbf{x}_p) {}^w \mathbf{x}_p + d_{22} (\mathbf{f} \cdot \mathbf{z}_p) {}^w \mathbf{z}_p \end{aligned} \quad (2.105)$$

Both components of the desired velocity are written on the basis of the principle components. By replacing equations 2.103 and 2.105 in equation 2.94 we have:

$${}^w \mathbf{V} = d_{11} (\mathbf{f} \cdot \mathbf{x}_p) {}^w \mathbf{x}_p + d_{22} (\mathbf{f} \cdot \mathbf{z}_p) {}^w \mathbf{z}_p + e_{11} \Omega {}^w \mathbf{x}_p \quad (2.106)$$

Therefore, non of the component of the velocity will change when the microrobot rotates around the central axis.

Since $\|\mathbf{V}_{hor}\| \neq 0$, as it is shown in the Fig 2.12 we can define the angle α between the vector \mathbf{v} and the vertical axis in the world frame.

$$\alpha = \tan^{-1}(\|\mathbf{V}_{hor}\| / \|\mathbf{V}_{ver}\|) \quad (2.107)$$

The microrobot is required to be in a position above the desired velocity vector (upward) with the angle ψ to compensate for the gravity vector. If we project the desired velocity equation (2.106) into principle coordinate axis then we have:

$$(\mathbf{V} \cdot \mathbf{x}_p) = d_{11} (\mathbf{f} \cdot \mathbf{x}_p) + e_{11}\Omega \quad (2.108)$$

$$(\mathbf{V} \cdot \mathbf{z}_p) = d_{22} (\mathbf{f} \cdot \mathbf{z}_p) \quad (2.109)$$

As can be seen in the Fig 2.12, both sides of the equation 2.109 can be replaced by its equivalents:

$$(\mathbf{V} \cdot \mathbf{z}_p) = -\|\mathbf{V}\| \sin(\psi) \quad (2.110)$$

$$(\mathbf{f} \cdot \mathbf{z}_p) = \|\mathbf{f}\| \sin(\psi - \alpha) \quad (2.111)$$

Thus, the replaced equation will lead to the following:

$$-\|\mathbf{V}\| \sin(\psi) = d_{22} \|\mathbf{f}\| \sin(\psi - \alpha) \quad (2.112)$$

by applying the subtraction law for $\sin(\psi - \alpha)$ ⁸, the angle ψ can be obtained from the following equation:

$$\psi = \tan^{-1} \frac{(d_{22} \|\mathbf{f}\| \sin(\alpha))}{\|\mathbf{V}\| + d_{22} \|\mathbf{f}\| \cos(\alpha)} \quad (2.113)$$

⁸ $\sin(\psi - \alpha) = \sin(\psi) \cos(\alpha) - \cos(\psi) \sin(\alpha)$

All the parameters in the above equation are known and the direction point ($\tilde{\mathbf{X}}$) of the microrobot can be reconstructed by using angles α and ψ and defining a dummy vector $\tilde{\mathbf{V}}$ such that $\tilde{\mathbf{V}} = \tilde{\mathbf{V}}_{ver} + \tilde{\mathbf{V}}_{hor}$ where $\tilde{\mathbf{V}}_{ver} = -\|\tilde{\mathbf{V}}_{hor}\| \tan(\pi/2 - \alpha + \psi) \hat{\mathbf{g}}$ and $\tilde{\mathbf{V}}_{hor} = \mathbf{V}_{hor}$. Therefore the final solution for the direction point is:

$$\tilde{\mathbf{X}} = \frac{\tilde{\mathbf{V}}}{\|\tilde{\mathbf{V}}\|} \quad (2.114)$$

Therefore the angular velocity (Ω) will be derived from equation 2.108, considering that $(\mathbf{V} \cdot \mathbf{x}_p) = \|\mathbf{V}\| \cos(\psi)$ and $(\mathbf{f} \cdot \mathbf{x}_p) = -\|\mathbf{f}\| \cos(\psi - \alpha)$:

$$\Omega = \frac{\|\tilde{\mathbf{V}}\| \cos(\psi) + d_{11} \|\mathbf{f}\| \cos(\psi - \alpha)}{e_{11}} \quad (2.115)$$

At this point the rotational velocity of microrobot can be used to compute the magnetic torque according to the following equation from propulsion equation system;

$$\tau = \mathbf{B} \mathbf{V} + \mathbf{C} \Omega \quad (2.116)$$

Where \mathbf{V} is known and \mathbf{B} and \mathbf{C} are precomputed from coefficient matrix. The torque in the magnetic torque equation is replaced by its equivalent 2.116;

$$\tau = \mathbf{V} M \times \mathbf{B} \quad (2.117)$$

Where M magnetisation constant and V is a volume of the magnetic object. Finally, the electric current (i) is required to generate a dynamic magnetic field is achieved by the following;

$$|\mathbf{B}| = \left(\frac{b^2}{(b^2 + l^2)^{3/2}} \right) \mu_0 i \quad (2.118)$$

And the simulation algorithm is completed.

Chapter 3: Results

3.1 Simulation

The aim of implementing the simulation framework for a microhelix is to analyse the effect of the key parameters on a microhelix's performance. As the microhelix moves in a fluid environment, modelling its swimming motion is one aspect of the implementation.

Simulation software Initially, Matlab was selected as the simulator software. However, after exploring the different aspects of the simulation, it became evident that the limitations of the software made it impossible to develop a complete simulation framework. One of the limitations was inability of the software to incorporate and bind all the physics involved in this modelling. Furthermore, Matlab was incapable of considering all aspects of a fluid environment. Therefore, another simulation software called COMSOL was used to implement the model. Although, COMSOL offers many build in environment that helps to make our simulation model, implementing an entire framework was required many considerations.

Model components The system configuration (figure 3.1) is based on the experimental setup run by Mahoney et al.. Although the experiment was run on a mili-robot, they used three inset Helmholtz coils to generate a magnetic field for microrobot actuation. The table 3.1 represents the details of the Helmholtz coils which generates a dynamic magnetic field by using AC current.

The size of fluid box is $25(\text{mm}) \times 25(\text{mm}) \times 25(\text{mm})$ and the viscosity of fluid inside the box is $2000(\frac{\text{N}}{\text{m}^2}\text{s})$ which is the viscosity of the corn syrup.

Coil set	Coil radius (mm)	Number of wraps
Inner	44	63
Middle	69	99
Outer	98	143

Table 3.1: Simulation model configuration. The detail of three inset Helmholtz coils setup [7].

Simulation forms of two main parts; microhelix propulsion mechanism and its actuation method.

The model is made of three components;

- Three inset Helmholtz coils
- The fluid box
- The microhelix

In order to simplify the model, it was broken down into three sub-models. Each sub-model made of two components and the entire model made by combining three sub-models as shown in figure 3.1.

In each sub-model, the physics involve in its components were solved. For example, in sub-model 1 we studied the effect of the magnetic field on the fluid box without considering the microhelix inside the box. Defining an appropriate domain for the solution is an important factor in modelling because the magnetic field decays as the distance from the magnetic source increases. Thus, the sphere domain with the radius of 3cm defined to solve the model as it is shown in figure 3.2

The effect of microhelix design parameters such as helical angle on rotational velocity of microhelix was examined in a simulation. The considered parameters are;

- Helix angle

Sub-models	Helmholtz coils	Fluid box	Microhelix
1	✓	✓	
2		✓	✓
3	✓		✓

Table 3.2: Modelling Simulation Components. The table shows the components of each sub-model.

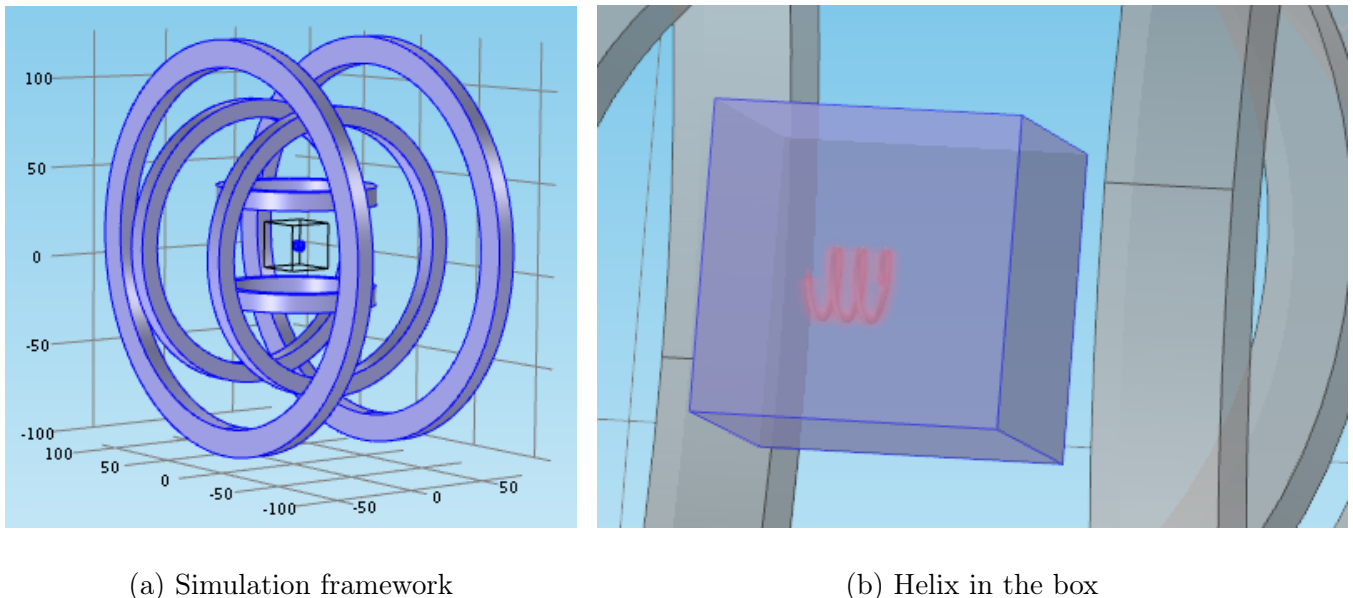


Figure 3.1: Simulation framework. (a) The framework consists of the three inset coils, a fluid box with a microhelix inside (b).

- Helix pitch
- Helix radius
- Helix filament radius

The result of each parameters effect on the rotational velocity of the microhelix is represented as follows. The curve in the figure 3.3 describes the relationship between the helical angle and rotational velocity. The helix with a small helical angle will generate a small rotational velocity as shown in the figure ???. However, the simulator does not respond to a helical angle greater

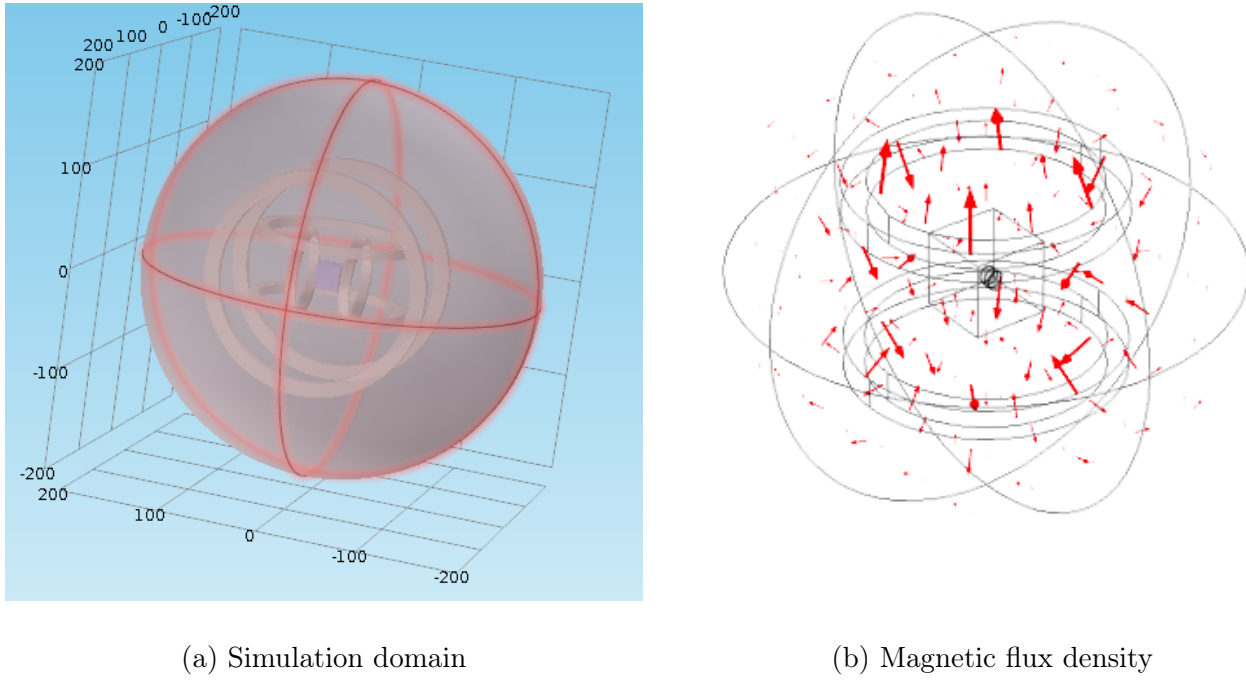


Figure 3.2: Simulation domain. (a) The sphere domain is defined for solving the model so the volume of effective magnetic flux in the model can be obtained (b).

than $1(\text{rad})$. Interestingly, for the zero helical angle, the simulator shows the rotational velocity just under $12(\text{rad/s})$. This confirms that in a extremely small helical angle RFT treats a helix as a cylinder. and therefore calculates a rotational velocity of a cylinder. Figure 3.4 describes the relationship between a rotational velocity of microhelix and its pitch. This curve shows an increase in rotational velocity by increasing a helix pitch. Figures 3.3 and 3.4 demonstrate the impact of helix radius and filament radius on rotational velocity respectively. Therefore, helical radius is more important than the filament radius.

The figure 3.5 describes the reverse relation between the helix radius and rotational velocity. As the radius of the helix is increasing the rotational velocity is decreasing, the highest rotational velocity is just above 14rad/s for the microhelix with $2\mu\text{m}$ radius. A similar behaviour is observed in figure 3.6 which is decreasing in rotational velocity by increasing the filament radius. However, the range of figures in the rotational velocity axis shows the helix filament radius only has a minor impact on the rotational velocity. Whilst, the considerable changes in rotational velocity occurs

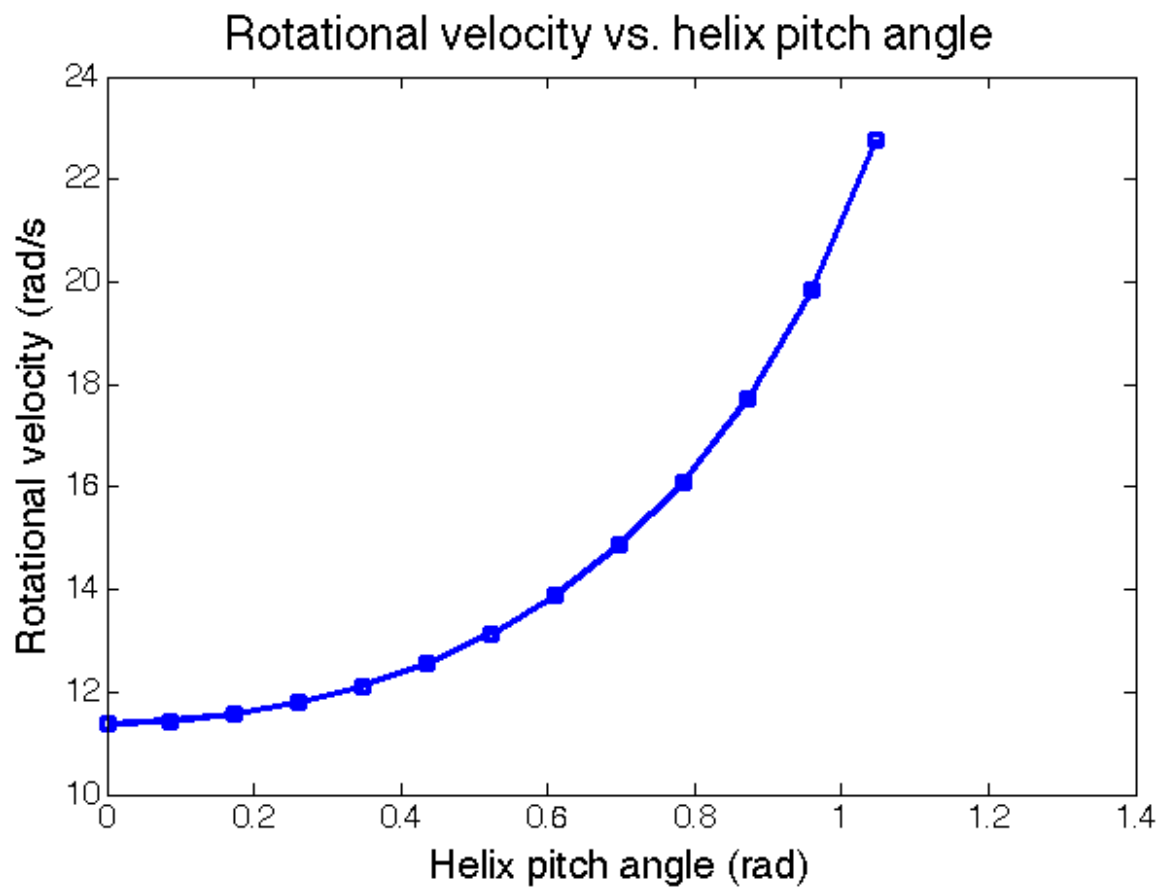


Figure 3.3: Rotational velocity vs. helix angle

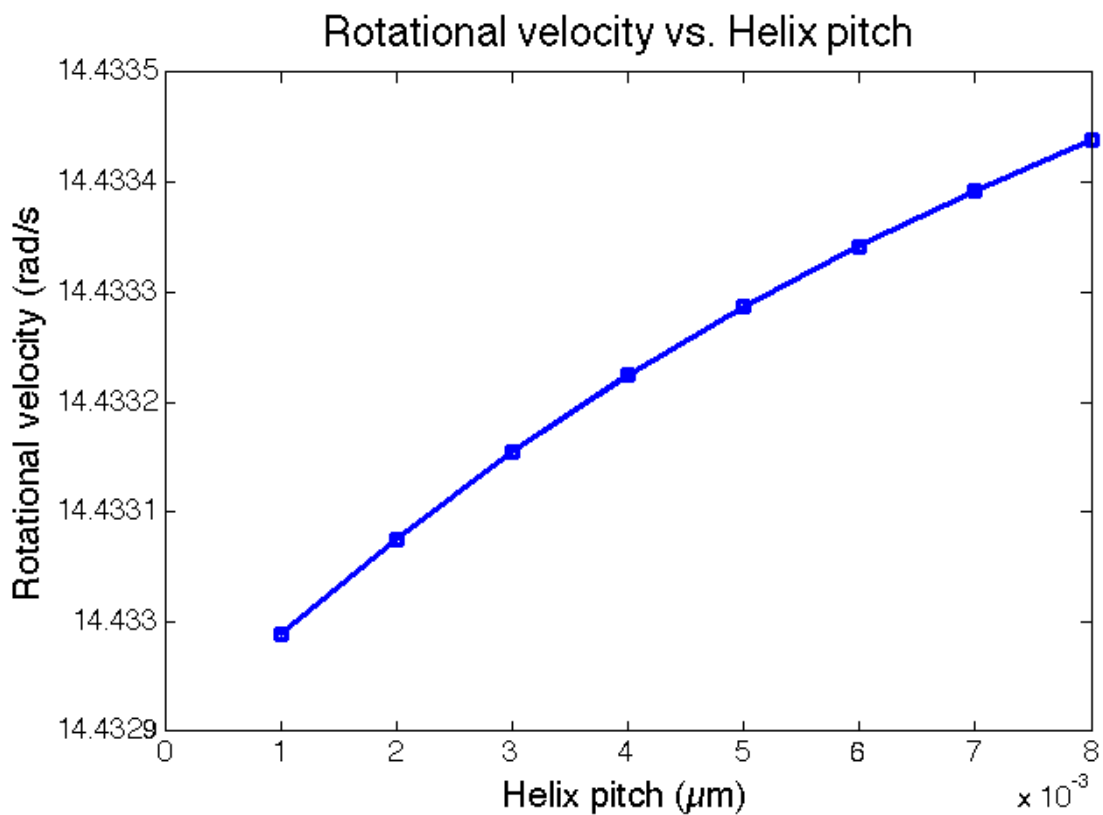


Figure 3.4: Rotational velocity vs. helix pitch

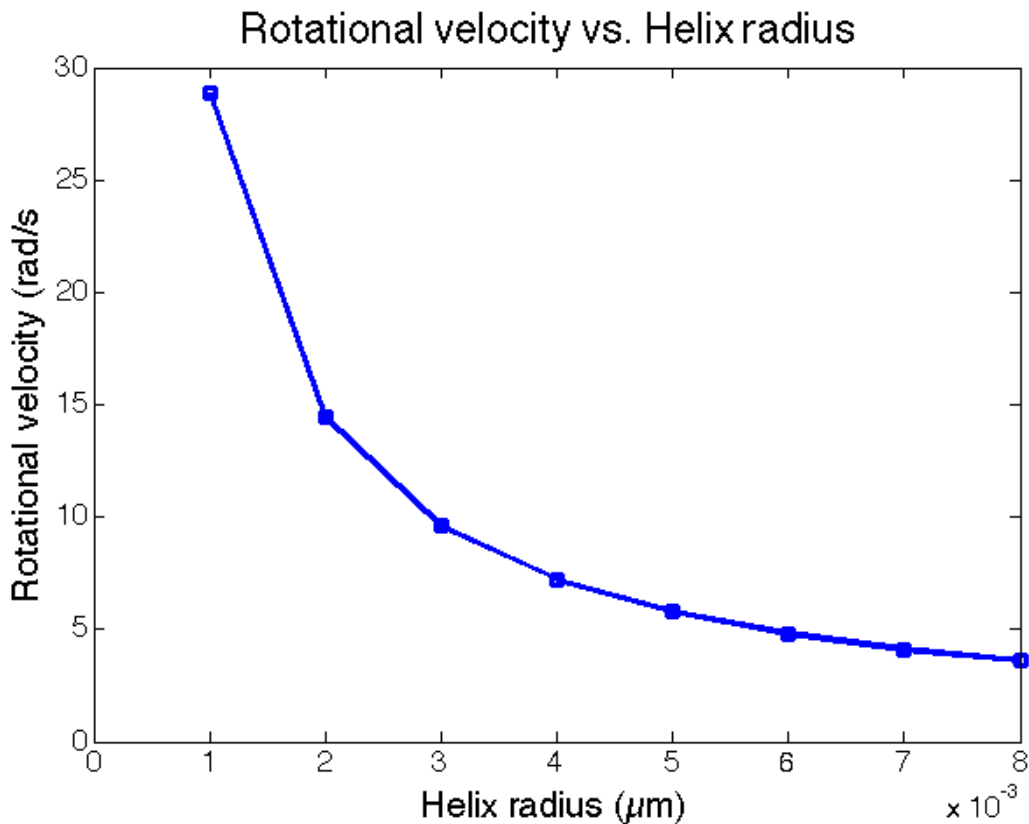


Figure 3.5: Rotational velocity vs. helix radius

by changing the helix angle and helix radius (figures 3.5, 3.3).

There is a linear relationship between rotational and translational velocity of microhelix as it is shown in figure 3.7.

3.2 Fabrication

The design of the microrobot in this study is focused on the microswimmer with helical shape tail and a possible propeller as the head that is attached to the helix body. Therefore, after studying the key characteristic of the helix and identifying effective parameters a series of designs were produced. We started by reproducing the previous design that had been made by other researchers in this field and finally proposed a new design for the helical shape microswimmers. The software called Solidwork has been used for designing and nanoscribe technology for the

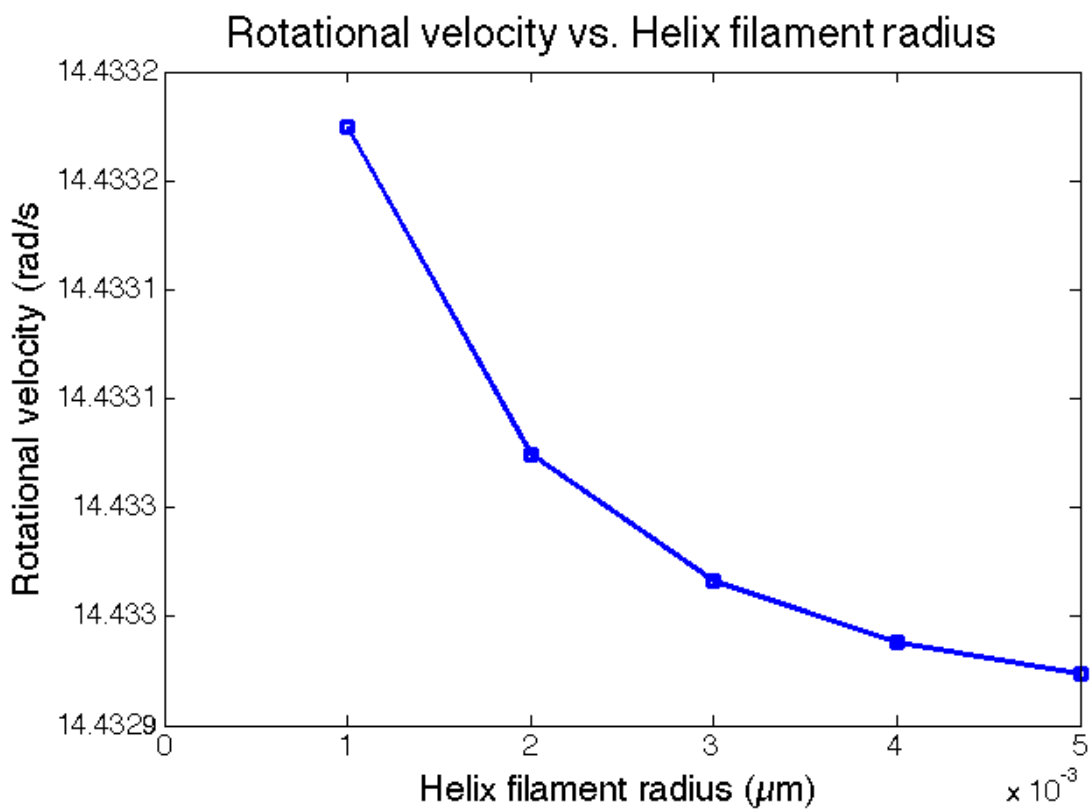


Figure 3.6: Rotational velocity vs. helix filament radius

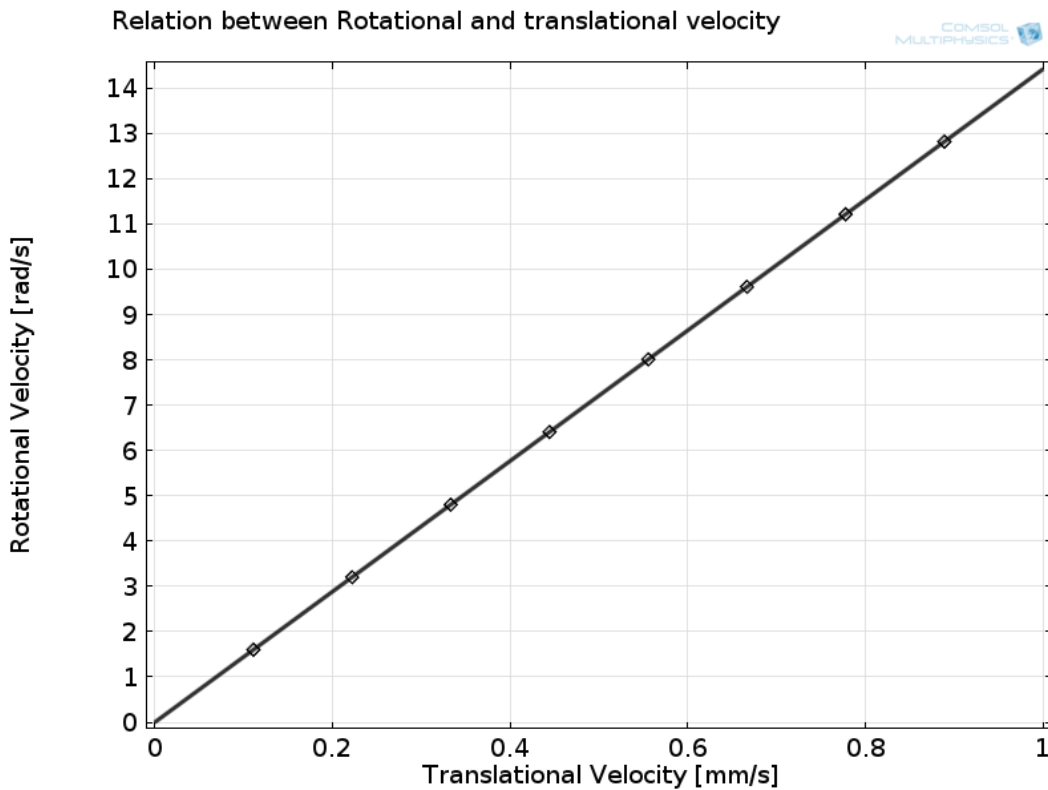


Figure 3.7: Rotational velocity vs. translational velocity. There is a linear realation between rotational and translational velocity.

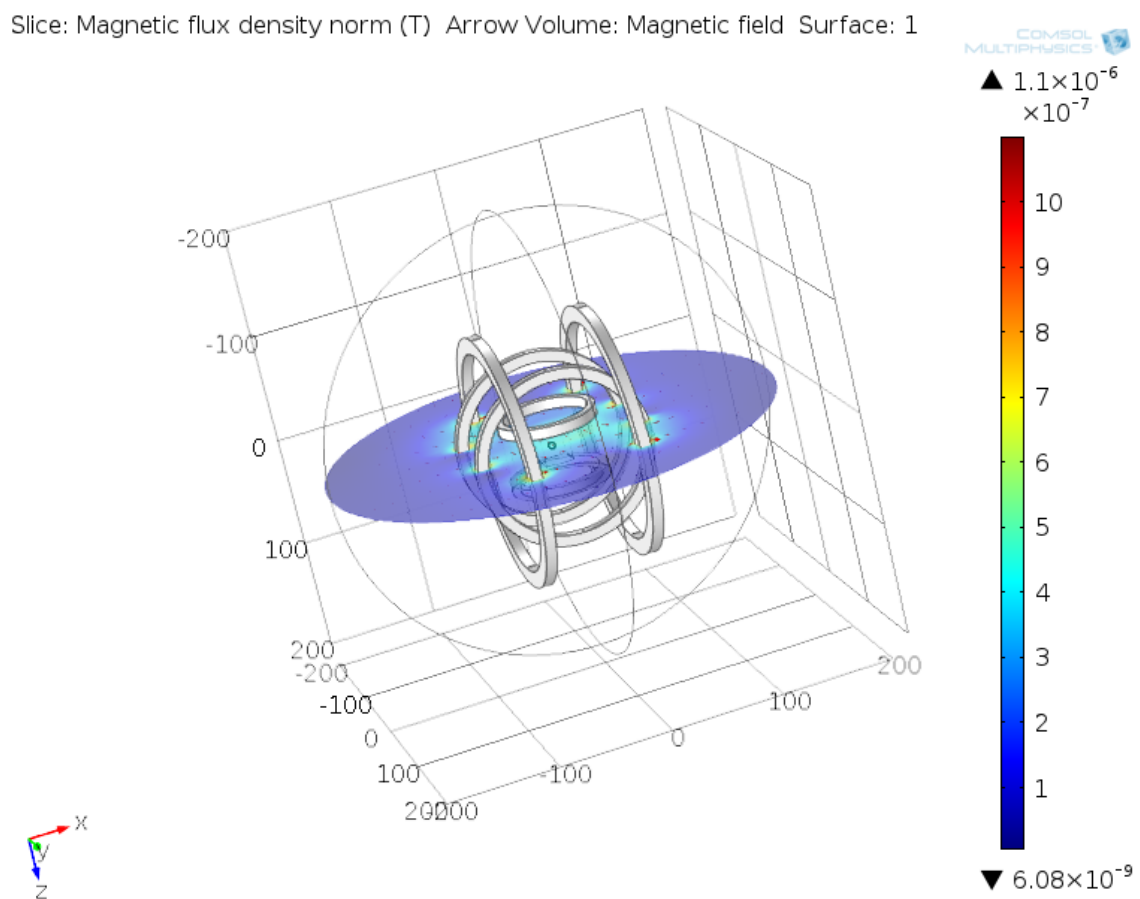
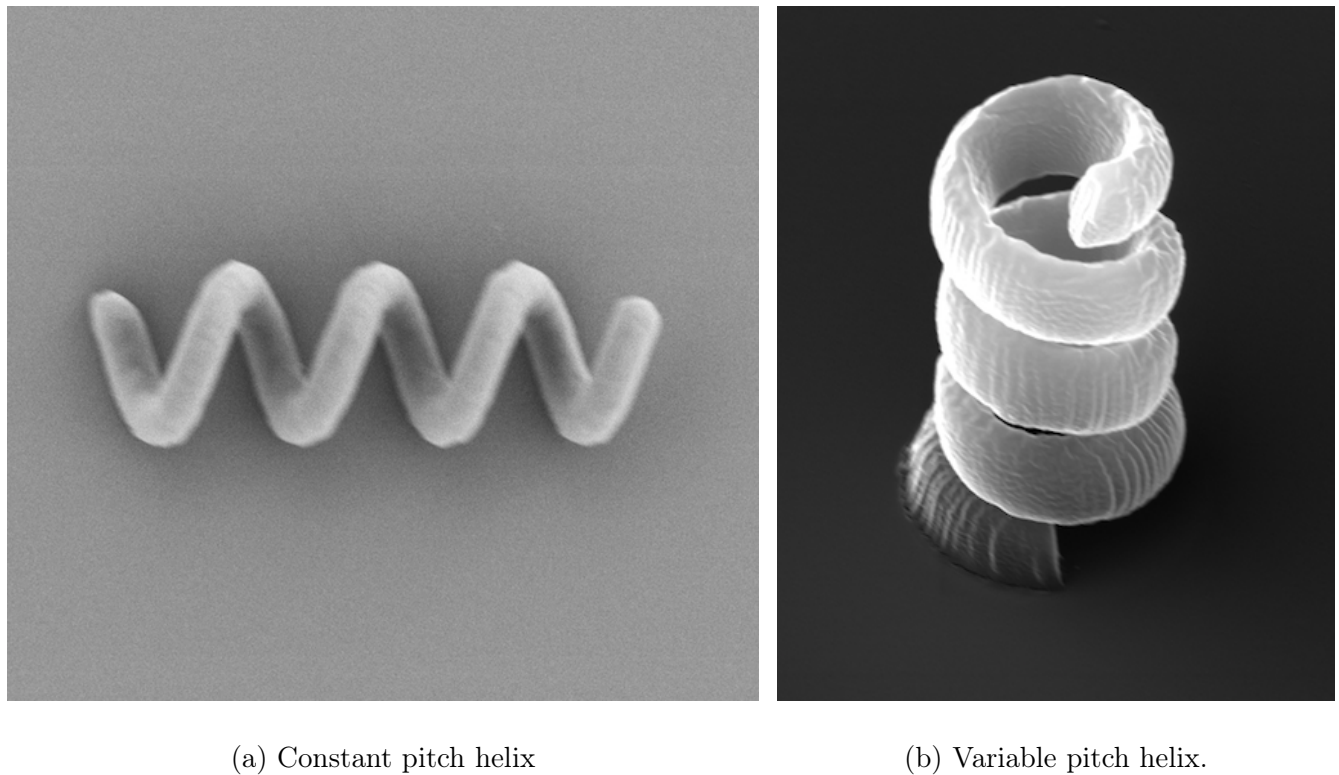


Figure 3.8: Microhelix first position. The simulator finds and positions the microhelix at the point of the strongest magnetic flux density.



(a) Constant pitch helix

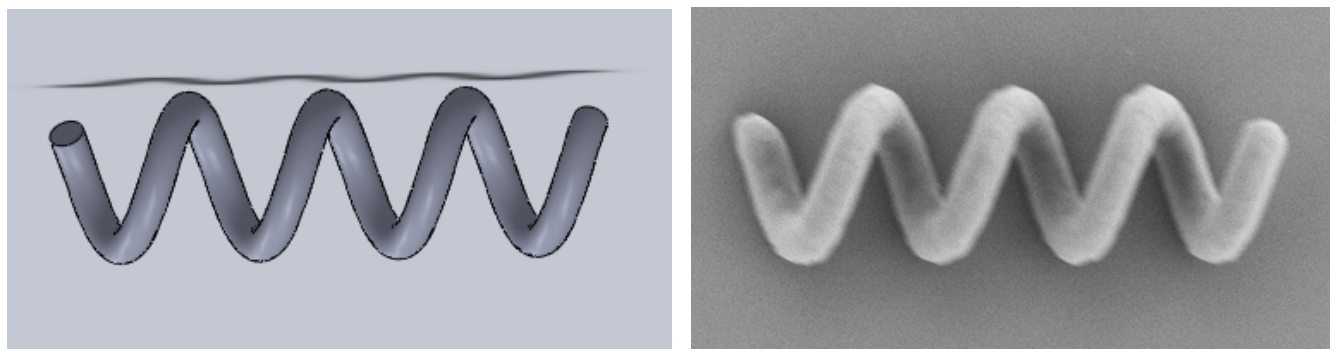
(b) Variable pitch helix.

Figure 3.9: Variable pitch helix. The image (a) is shown the constant pitch helix which could not printed vertically. However, the image (b) represents the successful vertically fabricated of (a) by making its pitch variable.

fabrication stage. In the following sections we present each design and the fabricated result.

Circle base filament A common design for the helix was one with a filament having a circular base. The designs vary in terms of changing the filament radius, helix pitch, helix length and helix radius. Some of the designs were successfully fabricated as shown in figure 3.10. The figure 3.11 presented a faulty result which is as result of either applying an insufficient or excessive power laser beam in the fabrication process. Also another type of faulty result can be seen in figure 3.11b which is due to excessive laser power.

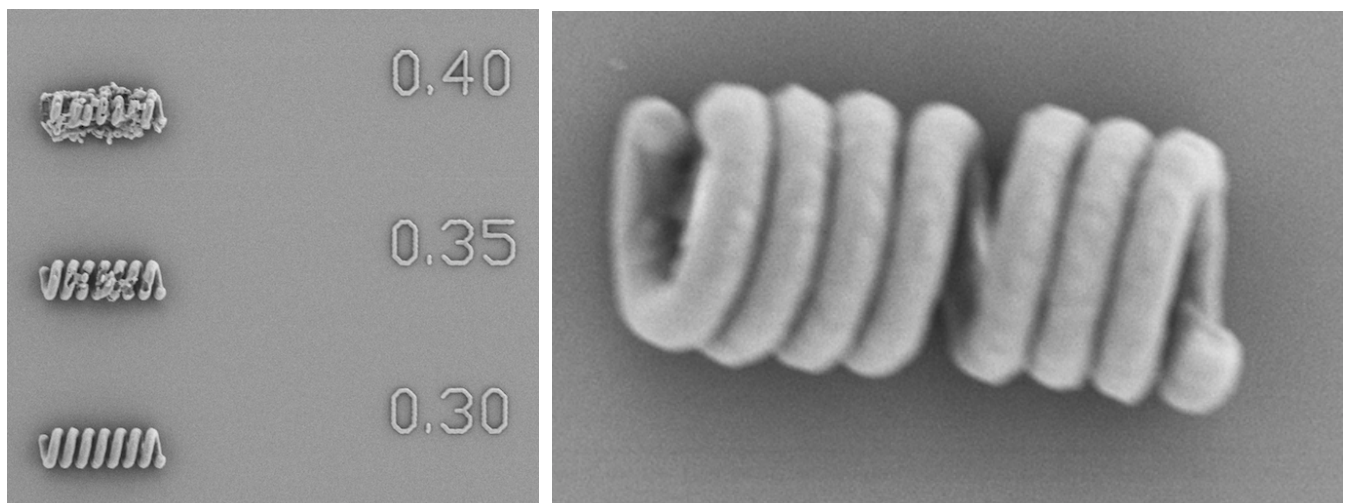
Rectangle base filament The second design has the rectangle base filament. This design can make two different helix shapes depending on which side of the rectangle is revolved around the spiral path in the design stage. The figure 3.12 shows a variety of designs based on the rectangle



(a) Design of circle base helix

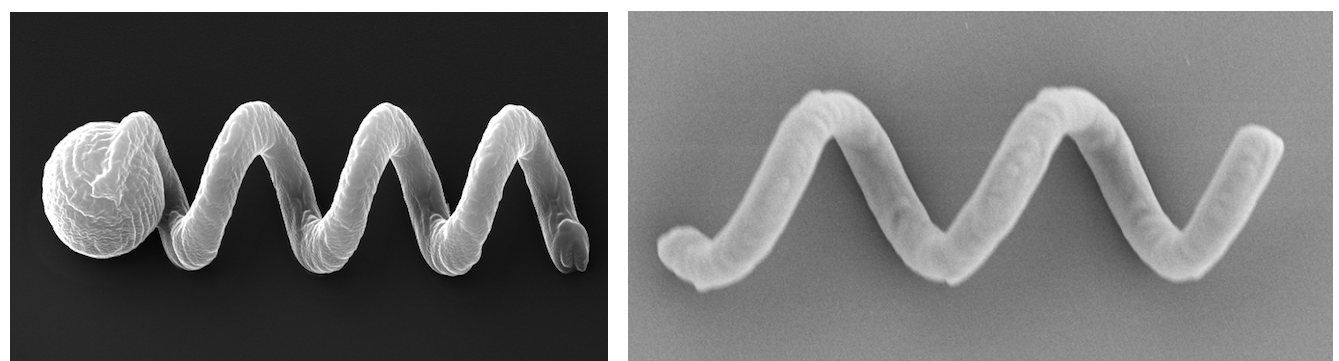
(b) Fabricated circle base helix

Figure 3.10: Circle base helix. This is the helix with $12\mu m$ length and $4\mu m$ pitch. (a) Helix in design stage and (b) shows the fabricated result.



(a) Damaged structure

(b) Small pitch helix



(c) Helix with a sphere head

(d) Large pitch helix

Figure 3.11: The structure (a) is damaged as a result of high laser beam and structure (b) has a small pitch $1.3\mu m$ and the result is not satisfactory. The structure with the sphere head (c) is fabricated and the helix with the larger pitch (d) is clearly shown,

filament with different pitch, length and helical radius.

Pitch variable helix In order to be able coat the structures with magnetic material, the structures should be printed vertically. The new helix design produced has a variable pitch. The problem with previous designs was that the starting helix angle from the bottom of the helix was too high. Therefore, the structure had a poor surface to rely on when in a vertical position. The first solution was producing structures with a small helix pitch to ensure a stronger base for vertical printing. However, as is shown in the figure 3.12f part (a) the overall result of the helix with the small pitch is not satisfactory. Thus, the idea of designing a helix with variable pitch enables us to meet both the simulation and fabrication requirements. The other advantage of having the variable pitch is providing a stronger base for a microhelix with an attached propeller. The result of the new design is shown in figure 3.9.

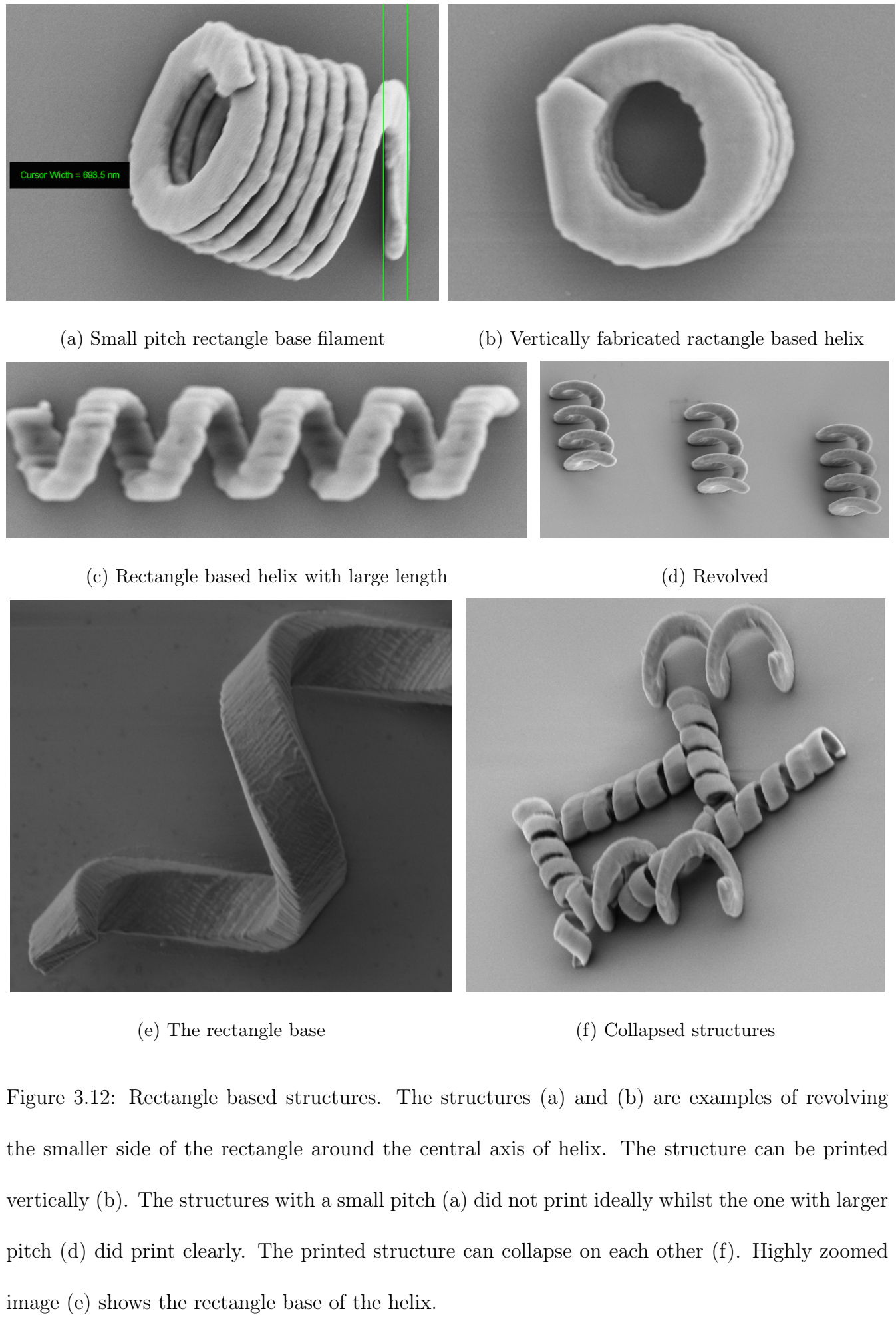


Figure 3.12: Rectangle based structures. The structures (a) and (b) are examples of revolving the smaller side of the rectangle around the central axis of helix. The structure can be printed vertically (b). The structures with a small pitch (a) did not print ideally whilst the one with larger pitch (d) did print clearly. The printed structure can collapse on each other (f). Highly zoomed image (e) shows the rectangle base of the helix.

Chapter 4: Discussion

The design of microhelix is based on the key characteristics of the helical shape. The circular shape was often used for the filament base of a helix. Therefore, the initial design was a helix with a circle base filament which was then integrated with different propeller heads such as a sphere and a square. Changing each characteristic one at a time and keeping the rest of the characteristics constant optimised the design of the microhelix. This algorithmic process was repeated for all new designs, such as a helix with a rectangle base filament. The helix design was optimised in terms of both fabrication and simulation.

In the fabrication process, the nanoscribe technology was used for 3D printing in micro size. This technology is based on lithography system to write a microstructure. The result of fabricated structures showed that the required laser power varies for printing each microhelix design. The result of horizontally printing microhelix was successful in many cases. However, in a few cases the microstructure collapsed because the laser power applied was either too high or too low. The appropriate amount of laser power was design dependent and so had to be varied for each design. In some cases the microstructure also collapsed during the developing process. The vertically fabricating microhelix was a challenge, as most of the design did not provide sufficient contact surface to support their weight. The new helix design with a variable pitch provided the structure with sufficient contact area with the substrate. The variable pitch helix has the smaller pitch at the bottom and a larger pitch over the rest of the body. As a result a small pitch at the bottom satisfies the vertically fabricated requirement of microhelix and larger pitch on the rest of the helix

body helps the swimming motion of the microhelix.

To model the swimming motion of the microhelix, three models were studied and RFT were implemented in the simulator. RFT has ignored the hydrodynamic interaction between the fluid flow produced by different segments of the microhelix. Therefore, in the microhelix with the smaller pitch the interaction between various parts of the helix increased and the helix is converted into a cylinder. This issue might result in an error when predicting the force and torque in a microhelix with an extremely small pitch. Thus, the variable pitch microhelix will help to avoid this issue.

To model the swimming motion of the microhelix three models were studied and RFT were implemented in the simulator. Each microhelix propulsion model segmented the filament of the microhelix differently. Then the model analyses an interaction of a small segment of the filament with the hydrodynamic characteristics of a high viscous fluid to achieve non fluidic force, torque and drag acting on a helix body. All three propulsion models were only applied to the microhelix with a circle base filament. Therefore, we will not be able to implement the propulsion model for other designs such as microhelix with a rectangle base filament.

Magnetic field is a safe power source to be used for actuating microrobot in the fluidic environment. There are advantages to applying torque driven magnetic field over force driven magnetic field, which makes it a preferable approach. Torque driven method can be applied on either microrobot with the flexible tail or a rigid tail. This method is more efficient than force driven as the rotation of helix leads to translational movement in the fluidic environment whilst the force driven method pulls the helix to generate the translational velocity.

Implementing the model using simulation software is a challenge. There is very few simulation software available that provide all the requirements of the model. Therefore, modelling the simu-

lator for microrobot navigation becomes more complex. For example the hydrodynamic property of the fluid and its effect on the swimming microrohelix cannot be modelled entirely with Matlab. COMSOL software offers more advanced simulation in terms of solving the multiphysics model by coupling the different physics. However, the modelling can be performed differently by coupling different components of the system.

Chapter 5: Conclusion and future work

The magnetically actuated helical shape microrobot has the advantage that it can be used in both in vivo or in vitro applications. Different microhelix shapes were designed, which included designs reproduced from previous researchers as well as new designs being presented. Of the latter group, the most successful new design was a helix with a variable pitch. This was because this design provided greater contact area with the substrate and this in turn enabled the structure to stand vertically during the fabrication process. The stronger base also gave the variable pitch design an advantage when attaching a propeller to the microrobot. The new design performed satisfactorily during the simulation process. The RFT was used as a locomotion model for simulating the motion of a remotely controlled microrobot. The other propulsion models presented are SBT and RSM, which also describe the motion of a microhelix but were also remotely controlled for the first time. According to the simulation results, the helix angle is the most important characteristic of the helix, in terms of its impact on rotational and translational velocity. The other characteristic of helix radius has a lesser impact. The fabrication process performed by nanoscribe facility and microstructures were observed under SEM. Initially Matlab was used for implementing the model and towards the end of the project the COMSOL Multiphysics software was used because of the limitations of Matlab in solving the model.

Future work In order to validate the results of this study we need to run an experiment in a laboratory to compare the result of the simulation with the experiment. The simulation framework

is needs to be further optimised in order to simulate microhelix in fluids with different viscosity. In terms of fabrication, the effects of using a combination of magnetic material for microhelix coating can be assessed. The ideal locomotion method for a microrobot requires further investigation.

The design of an advanced microrobot is application dependent. The possibility of actuating a microrobot with other power sources such as ultrasonic can be considered. Furthermore, the fundamental design of a microrobot can be integrated with other tools to build an advanced microrobot. The microhelix with its transport claw is already proposed and demonstrated their result in moving micro objects. A swarm of microrobots and a mechanism for controlling them individually will improve their performance. Therefore, researching current medical applications and limitations of such surgical tools can lead to more advanced microrobot designs for specific applications.

Bibliography

- [1] D Phil, FRS Ara Darzi, FREng Guang-Zhong Yang, and Hani Marcus. Robotics in key-hole transcranial endoscope-assisted microsurgery: A critical review of existing systems and proposed specifications for new robotic platforms. 2013.
- [2] Jon Edd, Sébastien Payen, Boris Rubinsky, Marshall L Stoller, and Metin Sitti. Biomimetic propulsion for a swimming surgical micro-robot. In *Intelligent Robots and Systems, 2003.(IROS 2003). Proceedings. 2003 IEEE/RSJ International Conference on*, volume 3, pages 2583–2588. IEEE, 2003.
- [3] Kathrin E Peyer, Soichiro Tottori, Famin Qiu, Li Zhang, and Bradley J Nelson. Magnetic helical micromachines. *Chemistry-A European Journal*, 19(1):28–38, 2013.
- [4] Famin Qiu, Li Zhang, Kathrin E Peyer, Marco Casarosa, Alfredo Franco-Obregón, Hongsoo Choi, and Bradley J Nelson. Noncytotoxic artificial bacterial flagella fabricated from bio-compatible ormocomp and iron coating. *Journal of Materials Chemistry B*, 2(4):357–362, 2014.
- [5] Kathrin E Peyer, Li Zhang, and Bradley J Nelson. Bio-inspired magnetic swimming micro-robots for biomedical applications. *Nanoscale*, 5(4):1259–1272, 2013.
- [6] Tian Qiu, John G Gibbs, Debora Schamel, Andrew G Mark, Udit Choudhury, and Peer Fischer. From nanohelices to magnetically actuated microdrills: a universal platform for

some of the smallest untethered microrobotic systems for low reynolds number and bio-logical environments.

- [7] Arthur W Mahoney, John C Sarrazin, Eberhard Bamberg, and Jake J Abbott. Velocity control with gravity compensation for magnetic helical microswimmers. *Advanced Robotics*, 25(8):1007–1028, 2011.
- [8] Bruce Rodenborn, Chih-Hung Chen, Harry L Swinney, Bin Liu, and HP Zhang. Propulsion of microorganisms by a helical flagellum. *Proceedings of the National Academy of Sciences*, 110(5):E338–E347, 2013.
- [9] Wei Gao, Xiaomiao Feng, Allen Pei, Christopher R Kane, Ryan Tam, Camille Hennessy, and Joseph Wang. Bioinspired helical microswimmers based on vascular plants. *Nano letters*, 14(1):305–310, 2013.
- [10] Soichiro Tottori and Bradley J Nelson. Artificial helical microswimmers with mastigoneme-inspired appendages. *Biomicrofluidics*, 7(6):061101, 2013.
- [11] Sangwon Kim, Famin Qiu, Samhwan Kim, Ali Ghanbari, Cheil Moon, Li Zhang, Bradley J Nelson, and Hongsoo Choi. Fabrication and characterization of magnetic microrobots for three-dimensional cell culture and targeted transportation. *Advanced Materials*, 25(41):5863–5868, 2013.
- [12] Soichiro Tottori, Li Zhang, Famin Qiu, Krzysztof K Krawczyk, Alfredo Franco-Obregón, and Bradley J Nelson. Magnetic helical micromachines: fabrication, controlled swimming, and cargo transport. *Advanced materials*, 24(6):811–816, 2012.
- [13] Kathrin E Peyer, Erdem C Siringil, Li Zhang, Marcel Suter, and Bradley J Nelson. Bacteria-inspired magnetic polymer composite microrobots. In *Biomimetic and Biohybrid Systems*, pages 216–227. Springer, 2013.

- [14] Edward M Purcell. The efficiency of propulsion by a rotating flagellum. *Proceedings of the National Academy of Sciences*, 94(21):11307–11311, 1997.
- [15] Wang Xi, Alexander A. Solovev, Adithya N. Ananth, David H. Gracias, Samuel Sanchez, and Oliver G. Schmidt. Rolled-up magnetic microdrillers: towards remotely controlled minimally invasive surgery. *Nanoscale*, 5:1294–1297, 2013.
- [16] Famin Qiu, Rami Mhanna, Li Zhang, Yun Ding, Satoshi Fujita, and Bradley J Nelson. Artificial bacterial flagella functionalized with temperature-sensitive liposomes for controlled release. *Sensors and Actuators B: Chemical*, 2014.
- [17] nanoscribe. nanoscribe @ONLINE, February 2014. URL <http://www.nanoscribe.de/en/>.
- [18] Purdue University. Scanning electron microscope @ONLINE, January 2014. URL <http://www.purdue.edu/ehps/rem/rs/sem.htm>.
- [19] Roger McFadden. A basic introduction to clean rooms @ONLINE, 2014. URL <http://www.coastwidelabs.com/>.
- [20] David J Smith. A boundary element regularized stokeslet method applied to cilia-and flagella-driven flow. *Proceedings of the Royal Society A: Mathematical, Physical and Engineering Science*, 465(2112):3605–3626, 2009.
- [21] A J Mestel. Biofluids lecture 3: Flagellar swimming, resistive force theory @ONLINE, January 2013. URL <http://www2.imperial.ac.uk/~ajm8/BioFluids/>.
- [22] Frank M White and Isla Corfield. *Viscous fluid flow*, volume 3. McGraw-Hill New York, 1991.
- [23] MJ Lighthill. Large-amplitude elongated-body theory of fish locomotion. *Proceedings of the Royal Society of London. Series B. Biological Sciences*, 179(1055):125–138, 1971.
- [24] Li Zhang, Jake J Abbott, Lixin Dong, Kathrin E Peyer, Bradley E Kratochvil, Haixin Zhang,

- Christos Bergeles, and Bradley J Nelson. Characterizing the swimming properties of artificial bacterial flagella. *Nano Letters*, 9(10):3663–3667, 2009.
- [25] Li Zhang, Jake J Abbott, Lixin Dong, Bradley E Kratochvil, Dominik Bell, and Bradley J Nelson. Artificial bacterial flagella: Fabrication and magnetic control. *Applied Physics Letters*, 94(6):064107, 2009.
- [26] George Dallas. Principal component analysis 4 dummies: Eigenvectors, eigenvalues and dimension reduction @ONLINE, October 2013. URL <http://georgemdallas.wordpress.com/2013/10/30/principal-component-analysis-4-dummies-eigenvectors-eigenvalues-and-dimension-reduction/>.
- [27] Harvey Mudd College. Eigenvectors and eigenvalues @ONLINE, November 2013. URL <https://www.math.hmc.edu/calculus/tutorials/eigenstuff/eigenstuff.pdf>.
- [28] Eric Weisstein. Eigenspace @ONLINE, August 2014. URL <http://mathworld.wolfram.com/Eigenspace.html>.
- [29] Eric Lauga, Willow R DiLuzio, George M Whitesides, and Howard A Stone. Swimming in circles: motion of bacteria near solid boundaries. *Biophysical journal*, 90(2):400–412, 2006.